Nanoscale disorder and local electronic properties of $CaCu_3Ti_4O_{12}$: An integrated study of electron, neutron, and x-ray diffraction, x-ray absorption fine structure, and first-principles calculations

Jin-Cheng Zheng,[1] A. I. Frenkel,[2] L. Wu,[1] J. Hanson,[1] W. Ku,[1] E. S. Božin,[1,3] S. J. L. Billinge,[1,3] and Yimei Zhu[1,*]
[1]*Department of Condensed Matter Physics and Materials Science, Brookhaven National Laboratory, Upton, New York 11973, USA*
[2]*Physics Department, Yeshiva University, New York, New York 10016, USA*
[3]*Department of Applied Physics and Applied Mathematics, Columbia University, New York, New York 10027, USA*
(Received 17 October 2009; revised manuscript received 26 February 2010; published 29 April 2010)

We report a combined experimental and theoretical study of $CaCu_3Ti_4O_{12}$. Based on our experimental observations of nanoscale regions of Ca-Cu antisite defects in part of the structure, we carried out density-functional theory (DFT) calculations that suggest a possible electronic mechanism to explain the gigantic dielectric response in this material. The defects are evident in atomically resolved transmission electron microscopy measurements, with supporting evidence from a quantitative analysis of the electron diffraction and DFT which suggests that such defects are reasonable on energetic grounds. To establish the extent of the defects, bulk average measurements of the local structure were carried out: extended x-ray absorption fine structure (EXAFS), atomic pair-distribution function analysis of neutron powder-diffraction data, and single-crystal x-ray crystallography. The EXAFS data are consistent with the presence of the nanoclustered defects with an estimate of less than 10% of the sample being disordered while the neutron powder-diffraction experiments place an upper of ~5% on the proportion of the sample in the defective state. Because of the difficulty of quantifying nanoscale defects at such low levels, further work will be required to establish that this mechanism is operative in $CaCu_3Ti_4O_{12}$ but it presents a nontraditional plausible avenue for understanding colossal dielectric behavior.

DOI: 10.1103/PhysRevB.81.144203 PACS number(s): 77.84.−s, 77.22.−d, 71.20.−b

I. INTRODUCTION

Extensive studies of perovskite $CaCu_3Ti_4O_{12}$ (CCTO) have been carried out in recent years due to its unusually high dielectric constant ($\varepsilon_0 \sim 10^5$) in kilohertz radio-frequency region[1–3] across a wide range of temperatures (ε_0 remains almost constant between 100 and 600 K). Although high static dielectric constant was observed in many ferroelectric or relaxor materials, such as $SrTiO_3$ (Ref. 4) and other related perovskite compounds,[5] such high dielectric constant is normally associated with a ferroelectric phase transition and is strongly temperature dependent. The temperature dependence of these dielectric properties significantly limits the application of the materials for wireless communication and microelectronic devices, therefore, there is significant technological interest in the development of new materials such as CCTO that exhibit a temperature-independent giant dielectric constant over a wide temperature range.

The intriguing dielectric properties of CCTO are not well understood. Density-functional theory- (DFT-) based calculations suggest that the dielectric constant of the ideal crystal should be about 40,[6] which is at least four orders of magnitude smaller than that observed experimentally.[1–3] As a consequence, the intrinsic nature of the dielectric behavior of CCTO has been challenged and many extrinsic models have been proposed, based on percolating or nonpercolating conducting layers and internal barrier layer capacitance (IBLC).[7] Such models might be plausible for polycrystalline materials which consist of a large number of grain boundaries that can act as either conducting or insulating layers for current to percolate. For single crystals, there exist no grain boundaries, thus the IBLC mechanism has to be based on other planar defects, such as twin boundaries. From a crystallographic point of view, it is probable to have twins in CCTO, nevertheless, the long-expected twin domains have never been observed in any form of CCTO.[8] Furthermore, in single crystal, sintered ceramic and thin films of CCTO, the type and density of the defects are very different,[8] yet all show similar dielectric behavior, the origin of which has become a long-standing mystery.[9]

In this work, we report our study to shed light on the mechanism of the unusual dielectric properties of CCTO, by using advanced characterization tools which include transmission electron microscopy (TEM) [quantitative electron diffraction (QED) and high-resolution transmission electron microscopy (HRTEM) imaging], synchrotron x-ray diffraction (XRD), x-ray absorption near-edge structure (XANES), extended x-ray absorption fine structure (EXAFS), neutron powder diffraction and atomic pair-distribution function (PDF) analysis, and first-principles calculations based on DFT. From electron diffraction and HRTEM and EXAFS, we find significant indication for off-stoichiometric nanoscale regions containing Cu-Ca antisite defects existing within the stoichiometric ordered matrix of the single crystal. DFT calculations show that the ordered and disordered phases possess different local electronic properties, which we suggest gives rise to the huge dielectric response in the system. Single-crystal x-ray diffraction and powder neutron diffraction with PDF analysis provide place an upper bound on the quantity of the sample in this state of ~5%. More work is required to establish that this mechanism is operative in CCTO, the electronic mechanism based on the presence of nanoscale regions of chemical disorder presents a different

 ©2010 The American Physical Society

approach to study the colossal dielectric-response property.

The rest of the paper is organized as follows. Description of methodology (i.e., experimental and theoretical methods) is given in Sec. II with the results presented in Sec. III. Discussions on the possible origin of the unusual dielectric response in CCTO based on our analyses are presented in Sec. IV with a brief summary being presented in Sec. V.

II. METHODS

Large single crystals of CCTO were made by S. Wakimoto of University of Toronto. The crystals were grown by the travelling-solvent floating-zone method in an image furnace. Details of the crystal growth have been published previously.[3] The same crystals were studied previously by neutron scattering and optical conductivity.[3] The size of the crystal rods for neutron scattering was about 1 cm with a diameter of about 3 mm and the size of the crystals for the optical inferred measurement about a 3 mm disks with 1 mm in thickness. The crystals used for the present study of TEM, XRD, and EXAFS, were cut from the large crystal batch.

A. Quantitative electron diffraction and imaging

The electron microscopy study including high-resolution imaging and quantitative diffraction was carried out using a 300 kV field-emission microscope with a postcolumn energy filter and a 200 kV aberration-corrected microscope with an in-column filter at Brookhaven National Laboratory (BNL). All images were recorded on a 14-bit charge-coupled device camera while diffraction data were on 20-bit imaging plates to improve the dynamic range of diffraction-intensity acquisition. TEM samples were prepared using a standard procedure, consisting of mechanical slicing, polishing, dimpling, and thinning. The final stage of the thinning involves 5 kV Ar-ion milling (Fischione Instrument) at 10° glancing angle and liquid nitrogen temperature. Extreme care was taken to avoid any damage during the sample preparation process.

Electron imaging covered a wide magnification range from $1000\times-2\,000\,000\times$. Low magnification was mainly used to search for areas of interest, including defects and domain interfaces. Two-beam diffraction conditions were used for image contrast analysis. High magnifications (200 000× and above) were used to retrieve local structural information, such as local symmetry and atomic disorder, based on many-beam phase-contrast theory. Qualitative and quantitative image analyses were assisted with high-resolution image simulation using BNL computer codes based on multislice algorithms.

To understand the bonding characteristics and valence-electron distribution in CCTO, a unique quantitative electron-diffraction approach, the paralleling recording of dark-field images (PARODI) method,[10–14] was used to accurately measure the structure factors of low-order reflections. The measurement is model independent. In the PARODI setting, we focus the incident electron beam above the sample, rather than on the sample as in conventional converged beam electron diffraction (cCBED),[15,16] thus illuminating an area of tens to hundreds of nanometers in diameter and generating a disk pattern of Bragg reflections. The intensity oscillation in each reflection, also called Pendellösung fringes or shadow images, reflects the change in incident-beam direction as well as thickness variation in the illuminated area.

The low-order structure factors were determined through a refinement procedure by comparing experiment with calculation based on Bloch-wave dynamic diffraction theory. The initial calculations usually start from electron structure factors (ESFs) of the procrystals [i.e., a hypothetical crystal with atoms having the electron distribution of free atoms; also so-called independent atom model (IAM)]. Then iterative calculations were carried out by adjusting values of structure factors until the difference between calculated and experimental patterns reaches minimum. To ensure that this minimum is not a saddle local minimum, we tested it by selecting several different starting points and recalculating structure factors iteratively until we reach the same lowest minimum. The structure factors obtained in this way are regarded as *measured* structure factors.

Although PARODI is more technically demanding than cCBED, there are several advantages[10–14] of using PARODI method for crystals with a large unit cell (as the case of CCTO): (1) many reflections can be recorded simultaneously, ensuring the same condition of the exposure and the crystallographic direction of the incident beam for all reflections; (2) the defocused beam minimizes possible radiation damage in comparison with cCBED; and (3) due to the strong dynamical coupling of the different diffracted beams, the data points in each reflection obtained from different thicknesses of the illuminated area are independent data sets, thus the ratio of the number of observations vs the number of variables is dramatically increased and the reliability of refinement process is enhanced subsequently. In the present study of CCTO, the electron-diffraction measurements were carried out at 90 K using a Gatan liquid N_2 holder as well as at room temperature (RT).

B. Synchrotron x-ray diffraction

The singly-crystal XRD was performed at beam line X7B at the National Synchrotron Light Source (NSLS), BNL. The wavelength ($\lambda=0.9222$ Å) was determined by the powder pattern of LaB_6, and other instrument parameters were determined using the program FIT2D.[17] A high-quality whisker (see below) with an estimated size of $0.05\times0.02\times0.05$ mm was cut from a large single-crystal piece of CCTO, then mounted on the end of a glass fiber with 5 min epoxy. The data were collected with a MAR345 image-plate detector. A set of different hemispheres of data were collected with different scan rates and scan ranges to obtain the largest possible range of intensities. The minimum d spacing was 0.92 Å (maximum q of 6.82). The intensities were extracted and merged from the image-plate data with the program suite HKL.[18] An additional oblique incidence correction was applied.[18] The traditional refinement was carried out with the SHELXTL program.[19]

Similar to the electron diffraction, the XRD experiments were also carried out at both room temperature and 90 K, using an Oxford Cryo-cooler system. The lattice parameters,

temperature factors, and atomic coordinates, and *A*-site disorder were refined. To obtain the best structure factors for the structure, we selected a crystal which had sharp spots and which had almost no diffraction that could not be attributed to a single crystal. However, several samples were rejected which had diffraction spots from multiple crystals and even powderlike rings. The process of "selecting" a good crystal for single-crystal diffraction study may preclude selecting a crystal which exhibits the defects observed from much smaller samples such as those with TEM or powder diffraction.

Electrons and x rays are complementary probes. Since x rays see total electron density in crystals, it is difficult for x rays to distinguish valence and core electrons if the number of core electrons is large. Stevens and Coppens proposed a simple suitability criterion[20] for charge-density analyses using x ray, $S=V/\Sigma n^2 \gg 5 \sim 0.1$ Å^3 e^{-2}, where V is the volume of the unit cell and n is the number of core electrons. For CCTO, $V=402$ Å^3, $\Sigma n^2=5280e^2$, $S=0.08$ Å^3 e^{-2}, which is much smaller than the typical values suitable for charge-density study using x rays. Thus, x rays may be extremely useful to retrieve the basic structure of CCTO, it may not the best method for studying its bonding characteristics and charge-density distributions. In addition, the proposed disorder of the Ca and Cu cations (see below) and the limited range of data we acquired would normally restrict the interpretation of the valence-electron distribution.

On the other hand, incident electrons interact with electrostatic potential, thus at small scattering angle they are more sensitive to valance-electron distribution than x rays due to the near cancellation of the scattering from the positive nucleus and negative electron charges.[21] Nevertheless, due to high energy of the incident electrons we use, usually only very limited low-index reflections ($\sin\theta/\lambda < 0.6$ A^{-1}) can be recorded with sufficient quality. We thus took the advantage of the *complementarity* of electrons and x rays by combining the measured structure factor of low-order reflections from electron diffraction and high-order reflections from x-ray diffraction as a full data set. Multipole refinement model of Hansen and Coppens[22] were then used to refine the measured structure factors for charge-density analysis via computer codes of VALRAY (Ref. 23),

$$\rho_{\text{atomic}}(\mathbf{r}) = P_{\text{core}}\rho_{\text{core}}(r) + P_{\text{val}}\kappa^3\rho_{\text{val}}(\kappa r) + \sum_{l=1}^{l\,\max} \alpha^3 R_l(\alpha r) \sum_{m=1}^{l} P_{lm\pm} Y_{lm\pm}(\theta,\phi), \quad (1)$$

where $\rho_{\text{core}}(r)$ and $\rho_{\text{val}}(r)$ are the spherical atomic core charge density and spherical valence charge density (monopole), respectively. P_{core} and $\rho_{\text{val}}(r)$ are the electron population of core and valence parts. The last term is the multipole contribution. The Roothaan-Hartree-Fock atomic wave functions[24] were used to describe the core and valence charge densities of isolated atoms.

C. X-ray absorption spectroscopy: XANES and EXAFS

X-ray spectroscopy measurements (both the XANES and the EXAFS), were carried out to probe the local structure and electronic properties of the CCTO powder grounded from the same single crystal that was used in other measurements described here. The details of the techniques using these x-ray spectroscopy methods to study local structure of materials can be found in Refs. 25–32. XANES experiments (beamline X11A at NSLS) were mainly focused on the Ti *K* edge to examine its possible off-center displacement while the EXAFS data were collected for all three cations (*K* edge of Cu, Ti at beamline X11A and Ca at beamline X15B, NSLS) to measure the cation short-range order. The EXAFS spectra were analyzed concurrently for all three edges by using UWXAFS package[33] that implements multiple data set refinement with a nonlinear least square fit of FEFF6 theory[34] to the data. All coordination numbers between the Ti, Cu, and Ca central atoms and their nearest neighbors, their bond lengths and the mean-squared disorder in the bond lengths were varied in the fit.

One of the unique advantages of EXAFS study is its sensitivity to the local coordination numbers of nearest neighbors and, therefore, short-range order of alloys, which can be analyzed with equal facility for ordered and disordered structures. Several constraints described below were applied to unlike pairs (Cu-Ca, Ti-Ca, and Ti-Cu) to minimize uncertainties in the best-fit values of the structural parameters and increase confidence in the results.[35] In CCTO, the coordination numbers of Ti-Cu and Ti-Ca bonds, $N_{\text{Ti-Cu}}$ and $N_{\text{Ti-Ca}}$, do not depend on the degree or randomness of the distribution of Cu and Ca in the $I3m$ lattice because the total numbers of these bonds in the sample must be in the ratio defined by a 3:1 stoichiometry, even if there are macroscopic compositional fluctuations. Thus, $N_{\text{Ti-Cu}}$ and $N_{\text{Ti-Ca}}$ were fixed in the fits to 6 and 2, respectively. Furthermore, Ti is a common atom in the titanate perovskite $A\text{TiO}_3$ lattice, and each *A* atom (i.e., Cu or Ca) must have eight Ti neighbors. Thus, the coordination numbers $N_{\text{Cu-Ti}}$ and $N_{\text{Ca-Ti}}$ were fixed to 8. There are two Cu-Ca bonds and four Cu-Cu bonds per Cu atom, i.e., $N_{\text{Cu-Ca}} : N_{\text{Cu-Cu}} = 1:2$ in the $Im\bar{3}$ structure. However, if the Ca and Cu atoms occupied their sites randomly, with the probabilities $\alpha_{\text{Ca}}=0.25$ and $\alpha_{\text{Cu}}=0.75$ (i.e., $N_{\text{Cu-Ca}}:N_{\text{Cu-Cu}}=1:3$), then the average numbers of Cu-Ca and Cu-Cu bonds would be $N_{\text{Cu-Ca}}=1.5$ and $N_{\text{Cu-Cu}}=4.5$ (since the second-nearest-neighbor coordination number of Cu must remain 6 in both cases). Thus, $N_{\text{Cu-Ca}}=2$ corresponds to the ideal ordered $CaCu_3Ti_4O_{12}$ system, and $N_{\text{Cu-Ca}}=1.5$ to the random alloy ($Ca_{0.25}Cu_{0.75}TiO_3$). Analogously, for Ca, in the ideal system the coordination numbers should be $N_{\text{Ca-Cu}}=6$ and $N_{\text{Ca-Ca}}=0$. In the random alloy, they should be 4.5 and 1.5, respectively. EXAFS measurement is sensitive to the variation in coordination numbers within such limits, and, using careful analysis employing multiple-edge, multiple data-set refinement, one can resolve between different possible models of short-range order in alloys.[27,30,35–37] Fits were also made using a model with no antisite defects for comparison.

As a result of all constraints applied to the structural variables in our EXAFS analysis, and performing concurrent refinement of the Cu *K*-, Ca *K*-, and Ti *K*-edge data, we had the total of 43 relevant independent data points and as few as 18 adjustable parameters in the fits.

D. Neutron powder diffraction and atomic pair-distribution function measurements

To search for further evidence of cation sublattice disorder as a bulk effect, we considered neutron powder-diffraction data, applying a PDF analysis to the data. CCTO has been the subject of a number of structural studies.[2,38–45] We therefore refined various models incorporating antisite defects similar to those observed in TEM and EXAFS measurements[46] against the existing data that were reported in Ref. 9. These are time-of-flight neutron powder-diffraction data collected at the Special Environment Powder Diffractometer (SEPD) at the Intense Pulsed Neutron Source (IPNS) at Argonne National Laboratory. The data were subsequently analyzed by Fourier transformation and atomic PDF analysis. Details of the data collection and analysis can be found in Ref. 9.

The strength of the PDF technique is that it takes into account both Bragg and diffuse scattering, and yields structural information on both long-range order and local structural disorder in materials. The PDF function $G(r)$ gives the number of atoms in a spherical shell of unit thickness at a distance r from a reference atom. It peaks at characteristic distances separating pairs of atoms and thus reflects the atomic structure.[47] Structural information is obtained from the PDF data through a modeling procedure similar to the traditional reciprocal-space-based Rietveld method.[48] However, it is carried out in real space and yields the local structure rather than the average crystal structure.[47] From the refinements, different structural information can be extracted, such as lattice parameters, average atomic positions and amplitudes of their thermal motion, atomic displacements, site occupancies, and magnitudes of local octahedral tilts. The PDF analysis reported here involves structural modeling using the program PDFGUI.[49] In cases where the average and local structure are the same (i.e., well-ordered crystals), the structural parameters obtained from Rietveld and PDF analysis are the same.[50] However, when the local structure deviates from the average structure the parameters from the PDF will reflect the local structure and the Rietveld parameters the periodically averaged values.

We focused on neutron-diffraction data because there is more contrast between the Ca(b_{Ca}=4.70 fm) and Cu(b_{Cu}=7.718 fm) scattering lengths than with x rays (f_{Ca}=20 and f_{Cu}=29, respectively). Replacing Cu on Ca sites and vice versa has the effect of changing the integrated intensity of peaks in the PDF associated with those positions, though the effects can be small.[51] The antisite defects will also result in displacive disorder of oxygen ions surrounding these sites so enlarged oxygen atomic displacement parameters (ADPs), (and to a lesser extent enlarged cation ADPs) would be consistent with the presence of such disorder.

E. First-principles calculations

The first-principles calculations were based on DFT.[52] We used both full potential and pseudopotential methods to calculate the structural, electronic, and magnetic properties of stoichiometric and off-stoichiometric (Ca-rich or Cu-rich) CCTO. For the pseudopotential calculations, we used the

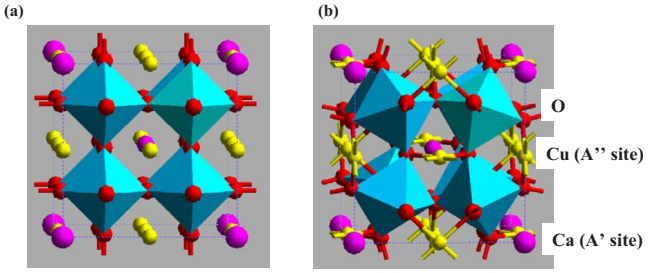

FIG. 1. (Color online) Structural model of CCTO. (a) Ideal perovskite structure and (b) with TiO_6 octahedra tilted.

SIESTA code[53] that is a fully self-consistent DFT method based on a linear combination of an atomic orbitals basis set with linear scaling. For full-potential calculations, we employed an augmented plane-wave plus local-orbital (APW+lo) method (implemented in WIEN2K package) (Ref. 54) in DFT framework. The configurations of spin ordering in the large unit cell (40-atom) for the stoichiometric and off-stoichiometric Ca-rich or Cu-rich CCTO were optimized by pseudopotential method, and then the related electronic and magnetic properties were obtained by full-potential calculations. Several types of exchange-correlation potential, such as local spin-density approximation (LSDA) (Ref. 55) and generalized gradient approximation [GGA–Perdew-Burke-Ernzerhof (PBE) (Ref. 56)], were employed. We also used the LDA+U self-interaction corrected[57] method to take into account the strongly correlated effects in CCTO.

III. RESULTS

A. Basic crystal structure

The space group of the ideal CCTO structure is $Im\bar{3}$ (No. 204 in the International Crystallography Table) in a primitive unit cell (20 atoms per cell), or $Pm\bar{3}$ (No. 200) in a more conventional unit cell used in the literature (a double primitive unit cell, 40 atoms per cell) to include the antiferromagnetic (AFM) ordering at Cu sites, as shown in Fig. 1. The cubic crystal cell has a lattice constant a=7.39 Å at 300 K with Wyckoff positions Ca(0,0,0), Cu(0,0.5,0.5), Ti(0.25,0.25,0.25), and O(0.3032, 0.1792, 0).[9] For the doubled unit cell, coppers with spin up (Cu1) and spin down (Cu2) are located at (0.5, 0, 0.5) and (0,0,0.5) sites, respectively, with a $Pm\bar{3}$ symmetry.

Our synchrotron x-ray diffraction data revealed a measurable difference in intensity between the 103 and 013 type of reflections (also 105 and 015, and the $h0l$ and $0hl$ family in general), suggestive of an untwinned crystal structure since a $Im\bar{3}$ crystal with twinning these reflections should be equivalent. This is consistent with our previous TEM studies.[8] Although early neutron and x-ray diffraction experiments suggested CCTO was twinned, an exhaustive search for twin domains or variants using various electron microscopy imaging and diffraction methods in single crystals, bulk ceramics, and thin films was unsuccessful.[8] It was argued that the failure of finding twinning using TEM is due to a scale issue since neutrons and x rays have a much larger beam size and

TABLE I. Summary of the refinement results by SHELXTL program. Temp=temperature, refl=reflections, R1=R factor 1, wR2=weighted *R* factor 2, GooF=goodness of fitting, Scale*=scale to bring F_{calc} (calculated structure factors) on the scale of the F_{obs} (observed structure factors).

Temp (K)	No. refl	R1	wR2	GooF	Scale*	Extinction parameter
300	58	0.023	0.075	1.32	0.490(8)	0.011(2)
90	53	0.019	0.082	1.48	0.489(9)	0.005(1)

if the twin domains in CCTO are larger than the electron-beam diameter one can easily miss them. It is important to note that modern electron microscopes offer a wide range of beam sizes, typically from 0.1 nm to 0.1 mm. This flexibility allows us to detect domains and defects of different length scales, thus revealing the symmetry of the crystal on different length scales, which may be lower than that observed by crystallographic x-ray or neutron experiment, which often probe with larger coherence volumes. Electron microscopists routinely use low magnifications, say 10 000×, to look for macroscopic structural features such as grains and twins based on diffraction or mass/thickness contrast in an electron microscope. If twin domains are 0.01 mm in size, then at 10 000× across the viewing chamber (20 cm×20 cm) of a microscope one would see two twin domains on the screen even without moving the sample (In fact, many microscopes can be operated down to 100x). Under various magnifications, using both imaging and diffraction modes in TEM, we have not observed twins in CCTO. (If the twin domains are smaller than 0.05 mm in size, we would not miss them.) We thus conclude that there exist no twins in CCTO, at least for all the samples we have examined. If the size of the twins is on the order of the crystal size, the low density of twins would have little effect on the properties of the materials. The absence of twins with appropriate sizes brings into question the applicability of the IBLC model for explaining the dielectric behavior of single-crystal CCTO.

Table I summarizes the refinement results of XRD using the SHELXTL program. In general, the fitting for space group $Im\bar{3}$ was quite good, especially for the strong reflections. A comparison between observed and calculated intensity of the Bragg reflections (structure factors squared) are shown in Fig. 2 for 300 and 90 K. Slight changes in lattice parameters are observed but no phase transitions are present in this temperature range. The temperature dependence of the structural parameters is quite small. For example, the coordinates of the oxygen atoms change in *x* and *y* directions are $0.1 \pm 0.16\%$ and $-0.2 \pm 0.3\%$, respectively, for a temperature range of 210 K. The change in the 141.5° bonding angle of Ti-O-Ti due to the tilt of TiO_6 octahedra (from the original 180° for the ideal cubic perovskite) with temperature is also very small, only 0.05° (namely, 0.04%) for $\Delta T = 210$ K. The structure factor obtained at 90 and 300 K was used for multipole refinement analysis and will be discussed in the following sections.

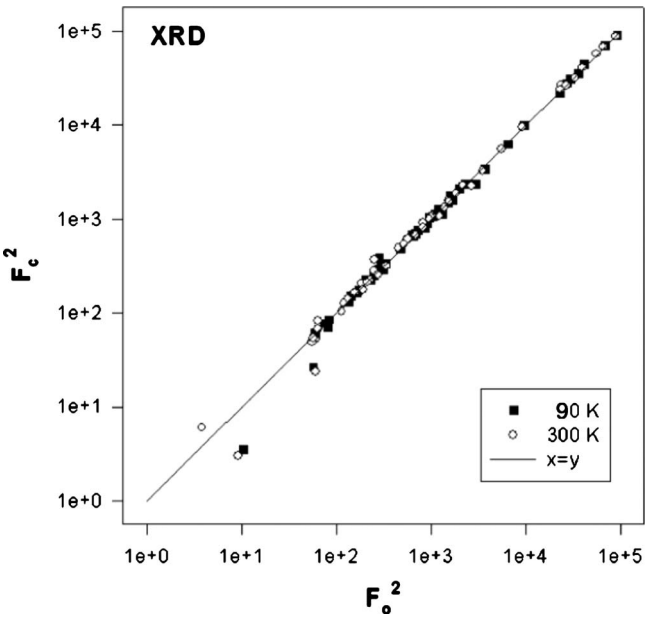

FIG. 2. Comparison of structure factor squared between calculation (F_c^2) and observation (F_0^2) in structural refinements using SHELXTL program. Solid square is for 90 K and open circle is for 300 K.

B. Low-order structure factors

1. Experimental measurements

Table II lists the nuclear charge, the atomic Debye-Waller factor, and the critical scattering vectors [s_c(Å^{-1})] for the element of O, Ca, Ti, and Cu that form CCTO. The critical scattering vector defines the scattering angle for a particular element below which the electron probe is more sensitive than x ray to measure the variation in the charge distribution.[21] In our electron-diffraction experimental setup, the scattering angle ($\sin\theta/\lambda$) of the six low-index reflections measurable with high accuracy (110, 200, 211, 220, 400, 422) all are smaller than s_c of Ca, Ti, and Cu (see Table III). Only the scattering vector of (422) reflection is larger than s_c of oxygen. This suggests it is crucial to use electron diffraction, rather than x ray, to accurately measure the structure factor of these six low-index reflections to understand the bonding characteristics and the valance-electron distribution in CCTO.

TABLE II. Atomic Debye-Waller Factor in CCTO at 90 K and 300 K, and estimated critical scattering vectors [s_c(Å^{-1})] from standard or parameterized tables of x-ray scattering factors for atoms (or ions).

			Debye-Waller factor	
Element	Nuclear charge	s_c	90 K	300 K
O	8	0.3	0.30	0.40
Ca	20	0.35	0.38	0.45
Ti	22	0.35	0.25	0.37
Cu	29	0.45	0.22	0.44

TABLE III. Electron-structure factors of the six innermost reflections in CCTO at 90 and 300 K, where experimental observations were compared with DFT calculations (LDA+U, U=4 eV) and a hypothetical crystal assembled by neutral atoms, namely, independent atom model (IAM) or procrystal. Please note the large deviation of the (110) structure factor between DFT calculation and experiment at 300 K, and the same calculated value at 90 and 300 K due to the insensitivity of the low-order reflection to atomic position and Debye-Waller factors. R_1 and R_2 are defined by Eqs. (2) and (3), respectively.

Index (hkl)	$\sin(\theta)/\lambda$ (Å)	T=90 K			T=300 K		
		ED measurements	LDA+U (U=4 eV)	IAM	ED measurements	LDA+U (U=4 eV)	IAM
110	0.09568	1.06 ± 0.12	1.17	3.38	0.63 ± 0.37	1.17	3.35
200	0.13531	−10.29 ± 0.42	−9.47	−11.50	−9.80 ± 0.19	−9.22	−11.53
211	0.16572	−3.21 ± 0.40	−2.76	−2.56	−2.93 ± 0.25	−2.67	−2.47
220	0.19135	48.92 ± 0.91	49.12	45.88	49.07 ± 2.18	48.90	45.66
400	0.27061	50.13 ± 1.32	50.58	50.05	47.44 ± 1.40	50.11	49.59
422	0.33143	37.56 ± 0.75	37.13	36.77	36.93 ± 1.05	36.57	36.22
R_1(%)			1.63	5.35		3.12	7.62
R_2(%)			5.80	43.23		17.91	79.75

As described in Sec. II A, the quantitative electron-diffraction (PARODI) approach was used for the measurements. An example of the experimental PARODI patterns of the h00 systematic row with 000, ±200, and ±400 reflections of CCTO is shown in Fig. 3(a). Please note the intensity oscillation in each disk is due to the dynamic scattering of incident electrons. Figure 3(b) is the comparison with the best-fit calculations. To simplify the analysis, we searched for a wedge area with a linear increase in thickness, t. In Fig. 3(a), the top-right edge of the reflection disks is the vacuum area (t=0) and the thickness of the illuminated area increases from top right to bottom left with t_{max}=170 nm. To keep the number of variables to a minimum, we only vary structure factors, crystal thickness (t_{max}), and crystal orientation in the fitting process. The line scans [as marked in (a)] of the experimental and calculated intensity profile from the same area, red lines and open circles, respectively, are plotted in Fig. 3(c), showing excellent agreement between experiment and calculation. The resulting six low-order ESFs from the fitting procedure are listed in Table III for two different temperatures, 90 and 300 K.

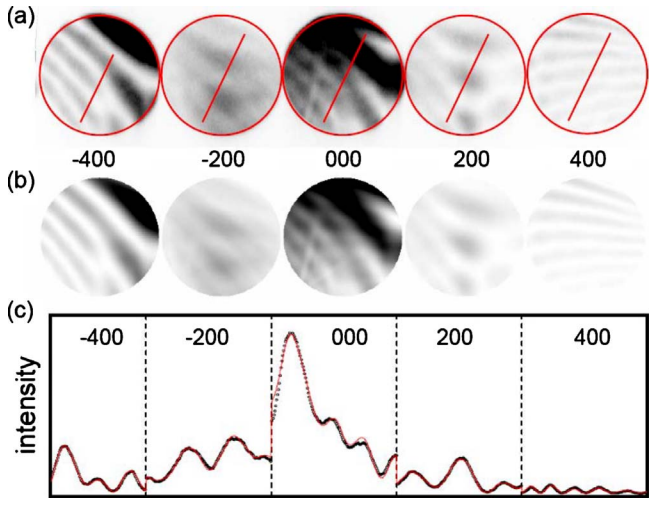

FIG. 3. (Color online) (a) Parallel recording of dark-field images (PARODI) of CCTO at h00 systematical row. (b) Calculation based on Bloch-wave method. (c) Line scan of the intensity profile from the experiment pattern in (a). The open circles are experiment while the red curves are calculation after refining the structure factors of 200 and 400.

2. Comparison of various theoretical approaches

Low-order structure factors are numerical parameters of a material property and very sensitive to chemical-bonding characteristics. Thus, they are very suitable for comparing and testing theoretical calculations from different models. In Table III, we also list the calculated ESFs using DFT (LDA+U) and IAM (independent atom model) corrected with temperature effects for 90 and 300 K.[9] The differences between calculated ESFs using DFT and IAM as well as measured ESFs are plotted in Fig. 4. The difference between ED measurements and DFT is in blue and IAM is in red in 90 K [Fig. 4(a)] and 300 K [Fig. 4(c)]. The sequence of the data points in the figure with the increase in scattering angle is (110), (200), (211), (220), (400), and (422) reflections. Figures 4(b) and 4(d) plot the relative changes in the ESFs in percentage, normalized by the ED measurements. Although the differences are somewhat reflection dependent due to the symmetry of the charge distribution, the trend is quite clear. The deviations from the experiment based on both IAM and DFT models are approaching zero at high scattering angles [(400) and (422) reflections] whilst being significant at small scattering angles. This is due to the fact that low-order ESFs are very sensitive to charge redistribution and bonding properties, due to the near cancellation of the scattering from the positively charged nucleus and the negatively charged electrons.[14,21]

The ESFs calculated by DFT are in better agreement with ED measurements than those calculated by IAM, as evidenced from Fig. 4 and the R factors [see Eqs. (2) and (3) below] in Table III. This is expected because in IAM calculations, the valence-charge rearrangements are totally ig-

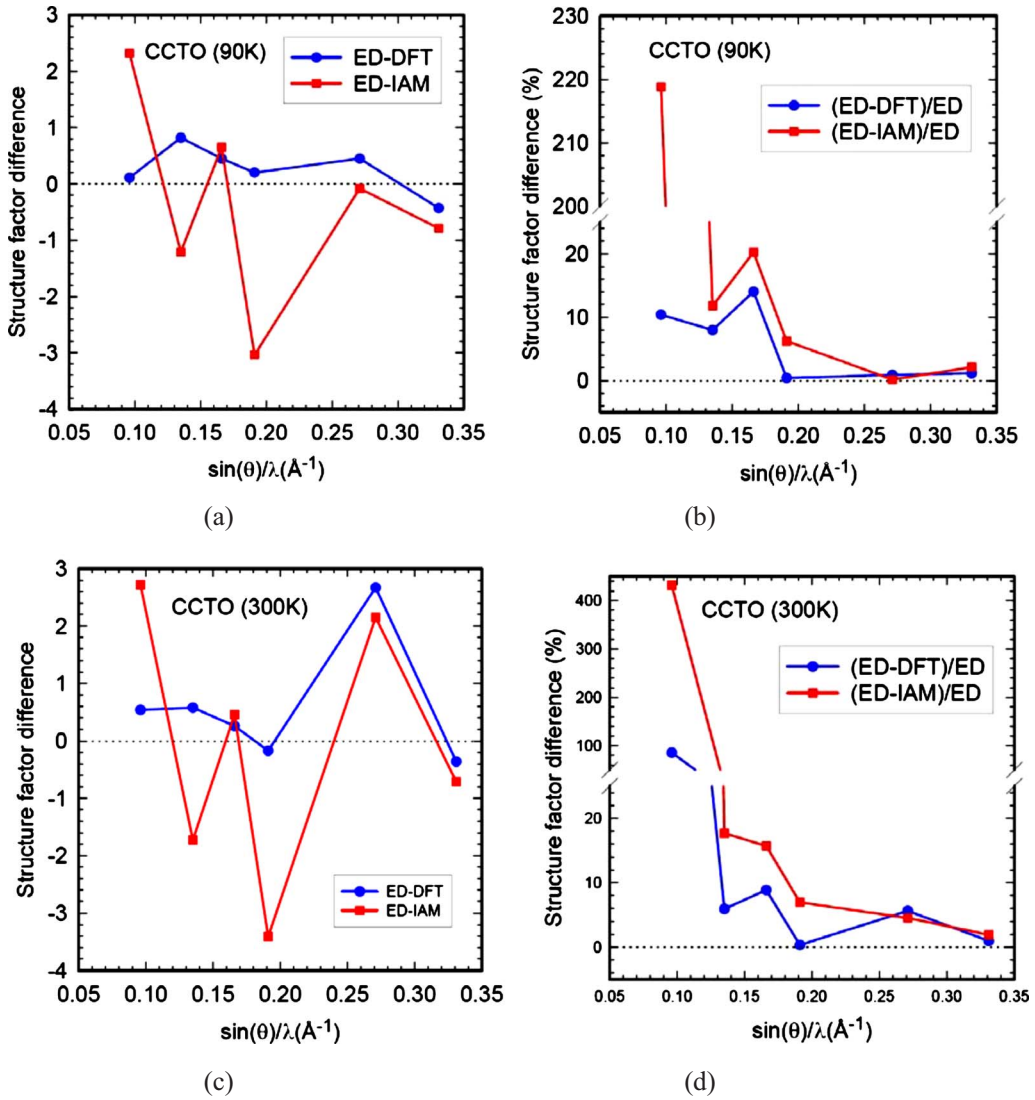

FIG. 4. (Color online) The difference of electron-structure factors of the six low-index reflections in CCTO obtained from different approaches for two different temperatures, (a)–(b): 90 K and (c)–(d): 300 K. (a) and (c): difference of structure factors between quantitative electron-diffraction (ED) measurements and density-functional theory (DFT) calculations (blue) and between ED and independent-atom-model (IAM) calculations (red). (b) and (d): relative changes in structure factor in percentage (%) normalized by the ED measurement. The sequence of data points in the figures from small to large scattering angle is (110), (200), (211), (220), (400), and (422) reflections.

nored while in DFT calculations, the valence-electron redistributions due to chemical bonding and charge transfer between ions are taken into account. The accuracy of ESF calculations by DFT depends on the approximations used for the exchange and correlation potentials, as well as the convergence control in calculations. The full-potential DFT calculations can give very accurate charge density in many complex systems including transition-metal oxides if strongly correlated effects are properly considered.

We further examine the effects on structure factors due to different magnetic configurations, i.e., paramagnetic (PM), ferromagnetic (FM), and AFM as well as exchange-correlation functionals (e.g., LDA or GGA). The results are listed in Table IV. In order to compare quantitatively these effects on ESFs, two different R factors were used. They were defined as

$$R_1 = \left(\sum_{i=1}^{n} |F^i_{(cal)} - F^i_{(\mathrm{ED})}| / \sum_{i=1}^{n} |F^i_{(\mathrm{ED})}| \right) 100(\%), \qquad (2)$$

$$R_2 = \frac{1}{n} \left(\sum_{i=1}^{n} |F^i_{(cal)} - F^i_{(\mathrm{ED})}| / |F^i_{(\mathrm{ED})}| \right) 100(\%), \qquad (3)$$

where $F^i_{(\mathrm{ED})}$ and $F^i_{(cal)}$ are ith measured and calculated (i.e., LDA+U or IAM) EFSs, respectively; and n is the number of ESFs. R_1, commonly used as goodness of fit,[58] is the summation of the differences between calculation and measurement divided by the total sum of measured ESFs. R_1 thus is more sensitive to the absolute values (and summation) of ESF differences, dominating for large values of ESFs, but not sensitive to relative changes in individual ESFs. It is

TABLE IV. Electron-structure factor of CCTO (40 atoms) calculated by DFT with 90 K lattice parameters and using 90 K Debye-Waller factor. [The experimental atomic positions are Ca(0,0,0), Cu(0,0.5,0.5), Ti(0.25,0.25,0.25), O(0.3028,0.1789,0) and the experimental lattice constant is 7.382 Å at 90 K.) PM: paramagnetic, FM: ferromagnetic, and AFM: antiferromagnetic.

(*hkl*)	GGA(PM)	LDA(PM)	LDA(FM)	LDA(AFM)
110	1.24	1.23	1.20	1.20
200	−9.12	−9.17	−9.16	−9.16
211	−2.74	−2.78	−2.79	−2.79
220	49.11	49.05	49.12	49.11
400	50.47	50.60	50.61	50.61
422	37.08	37.14	37.14	37.14
R_1(%)	1.87	1.81	1.85	1.84
R_2(%)	7.56	7.11	6.63	6.62

good for a large data set with large error bars such as those from x-ray measurements but is not sufficient to describe the characteristics in small data sets such as those obtained by ED even with much better accuracy. Therefore, in order to take into account the relative changes in every ESF, we also adopted R_2, as defined in Eq. (3), which is similar to the R factor we used previously.[21] The advantage of R_2 is that it treats the difference in percentage for each ESF equally, thus it is more sensitive to the relative changes in individual ESFs.

The differences in ESFs due to the different exchange-correlation functionals are within 0.1% for R_1, which are often smaller than the error bar in the experiment measurement. This suggests that LDA or GGA calculation result in very similar structure factors and charge densities in CCTO. Different magnetic configurations only give about 0.05% differences in R_1. The R_1 for LDA+U with an antiferromagnetic configuration has 1.63% deviation from ED measurements, adjusted for 90 K lattice constants and Debye-Waller factors (Table V). This is much smaller than the 5.35% from IAM. The R factors (R_1 and R_2) are slightly reduced with the increase in U in LDA+U until U reaches beyond 6 eV. This is consistent with the fact that CCTO is a strongly correlated

TABLE V. Effects of U in LDA+U on electron-structure factors (90 K lattice parameters) using 90 K Debye-Waller factor.

hkl	U=0 eV	U=4 eV	U=6 eV	U=8 eV
110	1.20	1.17	1.14	1.08
200	−9.16	−9.47	−9.46	−9.06
211	−2.79	−2.76	−2.75	−2.75
220	49.11	49.12	49.13	49.15
400	50.61	50.58	50.57	50.55
422	37.14	37.13	37.12	37.12
R_1(%)	1.84	1.63	1.63	1.85
R_2(%)	6.62	5.80	5.40	5.11

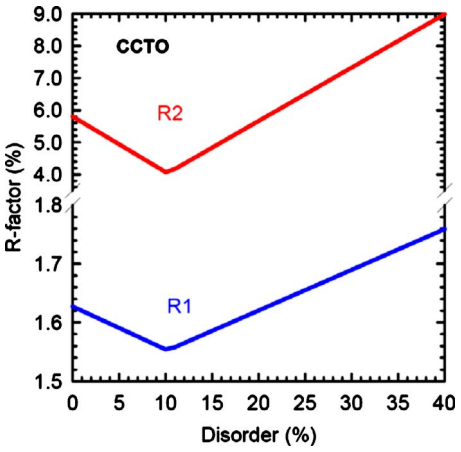

FIG. 5. (Color online) R factor as a function of Ca/Cu disorder in CCTO at 90 K. DFT calculations using LDA+U with U=4 eV.

system. For a comparison between experimental and calculated ESFs using the R_2 definition, the R factors are larger than R_1 because of the larger relative changes in SF of the (110), (211), and (200) reflections.

Overall, we found that, by comparing the R factors, improvement of exchange-correlation functionals (e.g., from LDA to GGA), the addition of strongly correlated effects (e.g., including U in LDA) or consideration of magnetic configurations (e.g., FM and AFM), does not improve the agreement between ED experiments and DFT calculations much. The discrepancy between the two with the best choice of U (U=4 eV) is still about R_1=1.6% (R_2=5.8%) at 90 K and R_1=3% (R_2=18%) at 300 K (Table III). This can be attributed the fact that the improvement of DFT calculations only gives about 0.2% reduction in R factors with the (110) structure factors being identical. This is because the low-order ESFs are not sensitive to the atomic positions, or the variation in temperature,[21] the more accurate determination of Debye-Waller factors will not further reduce the R factors. Nevertheless, at 300 K, the (110) ESF shows remarkable deviation from the calculation, in comparison with that at 90 K. Unexpectedly, when we induce 10% of Ca/Cu antisite disorder into the structure (see Sec. III D), the R factors of the six low-order ESFs are reduced considerably, R_2 reduced by 45% and R_1 reduced by 5%, as shown in Fig. 5. The improvement of the R factors at 300 K is more significant.[46] Due to the small value of the (110) ESF and large measurement error, the accurate assessment of the R factors improvement at 300 K is difficult to make but the trend is very clear. A few hundred percent of reduction in the R factors can be reached for room temperature if only the (110) reflection is considered.

C. Charge-density maps

Charge-density maps were obtained from multipole refinement of electron and x-ray structure factors. The latter are the Fourier component of the charge density. In our study, we combined structure factors of low-order reflections measured by electron diffraction with those of high-order reflections measured by x ray. Total 58 independent reflec-

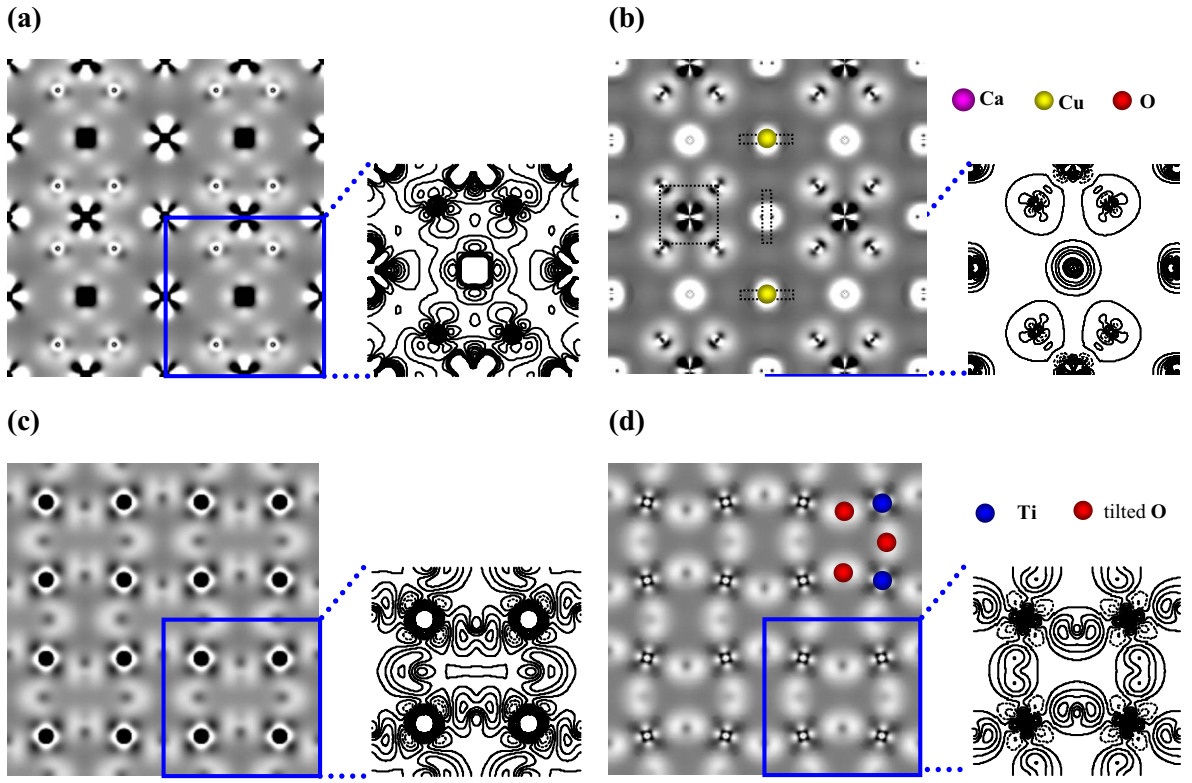

FIG. 6. (Color online) Deformation charge-density maps of CCTO derived from experimental measurements [(a) and (c)] and DFT calculations (LDA+U) [(b) and (d)] in the (001) planes for the Cu-Ca-O plane (z=0) in [(a) and (b)] and Ti-Ti plane (z=0.25) in [(b) and (d)]. The experimental results were obtained by combining structure factors of 58 reflections measured by electron diffraction (the six innermost reflections) and x-ray diffraction via multipole refinement. The square and rectangles in (b) represent the CuO_4 square in-plane and out-of-plane (with plane normal along the [100] and [010] direction. Enlarged contour plots from the marked area are shown on the right. Since in (d), the TiO_6 octahedra are tilted, the O atoms are not in the z=0.25 plane. Detailed comparison of the density map between experiment and calculation is not possible due to the limited number of reflections used in experiment (see text). The major feature in difference is the Ca site in (a) and (b): the calculation shows a close-shell orbital with a spherical symmetry while the experimental map shows some orbital anisotropy, suggesting possible Cu occupancy on the Ca site.

tions for 300 K and 53 for 90 K, corresponding to about 700 reflections if multiplicity is considered, were used to map the three-dimensional (3D) charge-density distributions in CCTO. Since total charge density is dominated by the core electrons which are not of great interest, we plot either valence-electron distribution if the core electron distribution is used as a reference or deformation map if the charge density of a procrystal (a hypothetical crystal formed by neutral atoms) is used as a reference. Figures 6(a) and 6(b) are the 90 K experimental deformation charge-density maps of CCTO in the (001) plane, the Cu/Ca-O basal plane (z=0) and the Ti-Ti plane (z=0.25), respectively, obtained after multipole refinements. For comparison, we also include those from DFT calculations within the local spin-density approximation (LDA+U) for ideal stoichiometric CCTO. The experimental map [Fig. 6(a)] clearly shows the bonding valence states, the electron density in the CuO squares and surrounding the Ca^{2+} ions in the basal plane (z=0). The magnetically active and orbital-ordered (OO) Cu d states exhibit well-defined t_{2g} symmetry [pointing toward the (110) directions], and form antibonds with neighboring O p states, in agreement with the calculation. Detailed comparison between experiment and calculation is not possible (details of the density map in calculation come from the infinitely large number of high-order reflections), due to the truncation error (limited number of reflections used) in experiment. We thus focus our attention on the main features, especially those extended to a large distance, in the distribution maps. As we can clearly observe in Fig. 6(a) that both experimental and calculated maps show open-shell d-electron orbitals for the Cu site with a fourfold symmetry. In contrast, at the Ca site, the calculation shows a close-shell orbital with a spherical symmetry while the experimental map shows some fourfold symmetry (orbital anisotropy with a weak e_g symmetry). This observation suggests possible 3d orbitals occupying on the Ca site, a result of local Ca and Cu switching or antisite disorder, as we reported previously. Although in our quantitative ED experiments, the probe size used was quite small ($<$5 nm), the areas of the crystal used for the measurement were rather thick ($\sim$100 nm). Should both ordered and disordered regions exist, we expect that the experimental map reflects an overlap of both. This is the significant outcome of our charge-density study. On the other hand, we did not observe any noticeable anomaly of the density map in the Ti-Ti plane (z=0.5). The agreement between experiment and calculation for the Ti sites [Fig. 6(b)] appears much better than Ca and Cu sites, suggesting less disorder for Ti.

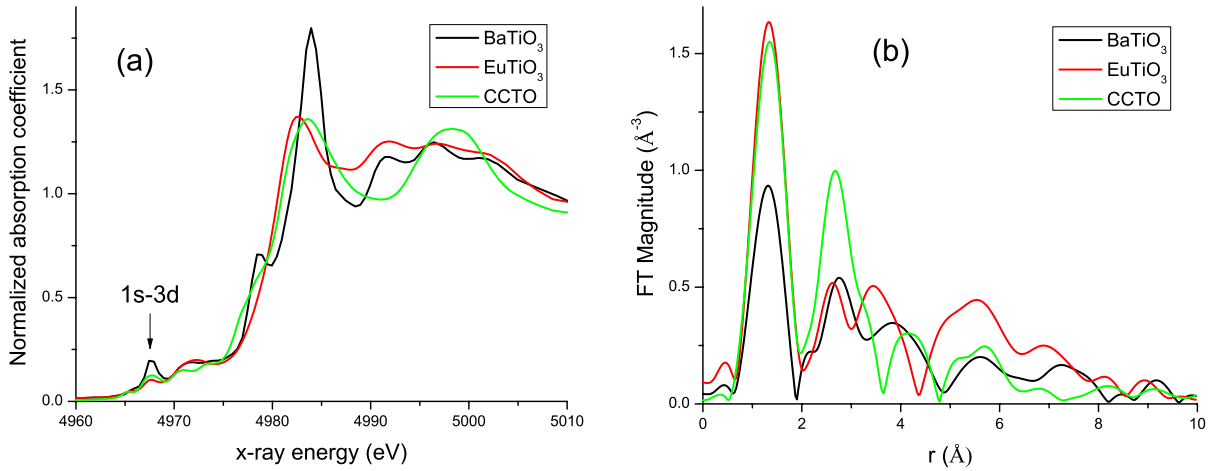

FIG. 7. (Color online) (a) XANES of Ti *K* edge in CCTO and two reference samples: $BaTiO_3$ (with 0.23 Å Ti atom static off-center displacement) and $EuTiO_3$ (with Ti atom being on the inversion symmetry center). The CCTO signal is similar to $EuTiO_3$ in the 1*s* 3*d* transition region, shown by the arrow. The nonzero signals in CCTO and $EuTiO_3$ are due to dynamic off-center displacements, which are much smaller than the static displacements in $BaTiO_3$. The $BaTiO_3$ and $EuTiO_3$ data are taken from Ref. 31. (b) Fourier-transform magnitudes of the Ti *K*-edge EXAFS. The magnitude in the first peak (corresponding to the first nearest-neighbor Ti-O contributions) is smaller in $BaTiO_3$ compared to $EuTiO_3$ and CCTO. In all cases, Ti is octahedrally coordinated by oxygens but in $EuTiO_3$, the disorder in Ti-O distances is purely thermal while in $BaTiO_3$, it is thermal and configurational (due to the split of six oxygens in two groups of three oxygens each); thus, the Debye-Waller factor term causes the signal in $BaTiO_3$ to be lower than in $EuTiO_3$. The similarity between the signal in $EuTiO_3$ and CCTO means that the Ti environment is also more symmetric in CCTO than in the room-temperature phase of $BaTiO_3$.

D. Local structure

1. Ti displacement

We examined the possible cation displacement in CCTO using synchrotron x-ray absorption spectroscopy by comparing CCTO with $BaTiO_3$ and $EuTiO_3$. It is well known that the off-center displacement of Ti ion in TiO_6 octahedron gives rise to ferroelectricity in $BaTiO_3$.[31] Ti is the most common "shifter" in titanate perovskites (e.g., $BaTiO_3$, $PbTiO_3$, $SrTiO_3$, and $EuTiO_3$). To study the possible Ti off-center displacement, we studied both XANES and EXAFS data in CCTO. Our XANES results demonstrate no enhancement (typical for systems with Ti off-center displacements) of the signal in the 1*s* 3*d* transition region (~4968 eV) below the Ti *K*-edge rise. The very presence of such a signal allowed in the past to evaluate the magnitude of such displacements in similar compounds.[26,30,31]

Figure 7(a) show the comparison of the Ti *K* edge in CCTO with two reference samples: $BaTiO_3$ (with 0.23 Å Ti atom static off-center displacement) and $EuTiO_3$ (with Ti atom being on the inversion symmetry center).[31] The CCTO signal is similar to $EuTiO_3$ in the 1*s* 3*d* transition region, as marked by an arrow. The nonzero signals in CCTO and $EuTiO_3$ are due to dynamic off-center displacements, which are much smaller than the static displacements in $BaTiO_3$. The $BaTiO_3$ and $EuTiO_3$ data are taken from Ref. 31. Our results suggest that Ti atoms are not displaced off-center of their oxygen coordination environments, which thus form relatively rigid structural units which can only rotate but not change their 3D shape. This is in agreement with a neutron PDF study which showed no evidence for Ti off-centering displacements in the local structure.[9] This is further supported by analysis of the Debye-Waller effects in the EXAFS. Figure 7(b) is the Fourier-transform magnitudes of the Ti *K*-edge EXAFS of the three samples. The magnitude of the first peak (corresponding to the first nearest-neighbor Ti-O contributions) is smaller in $BaTiO_3$ compared to $EuTiO_3$ and CCTO. In all cases, Ti is octahedrally coordinated by oxygens but in $EuTiO_3$, the disorder in Ti-O distances is purely thermal while in $BaTiO_3$, it is both thermal and configurational (due to the split of six oxygen atoms in two groups of three atoms each); thus, the Debye-Waller factor term causes the signal in $BaTiO_3$ to be lower than in $EuTiO_3$. The similarity between the signal in $EuTiO_3$ and CCTO suggests that the Ti environment is also more symmetric in CCTO than in the room-temperature phase of $BaTiO_3$. We thus conclude that there is no significant off-center Ti displacement in our CCTO single crystals.

The possibility of displacements of Cu and Ca atoms was also investigated using their *K*-edge XANES data. No evident off-center displacement of either Cu or Ca was observed. For the possible swap of Ca and Cu due to the local disorder, the Cu-O environment can be strongly disordered and one might expect that on the Ca site, due to its small size, Cu would not be located at the center of the Ca site. However, we did not gather any evidence of a preferred direction of Cu displacement: such evidence will be obtained by our EXAFS analysis.

2. Antisite (Ca/Cu) disorder

To further explore local disorder suggested by the charge-density study (Sec. III C), we conducted an EXAFS study. EXAFS reveals information about the short-range-order environment around selected atoms, including the number of their nearest neighbors, their types, average bond lengths, and their mean-squared relative displacements. Figure 8

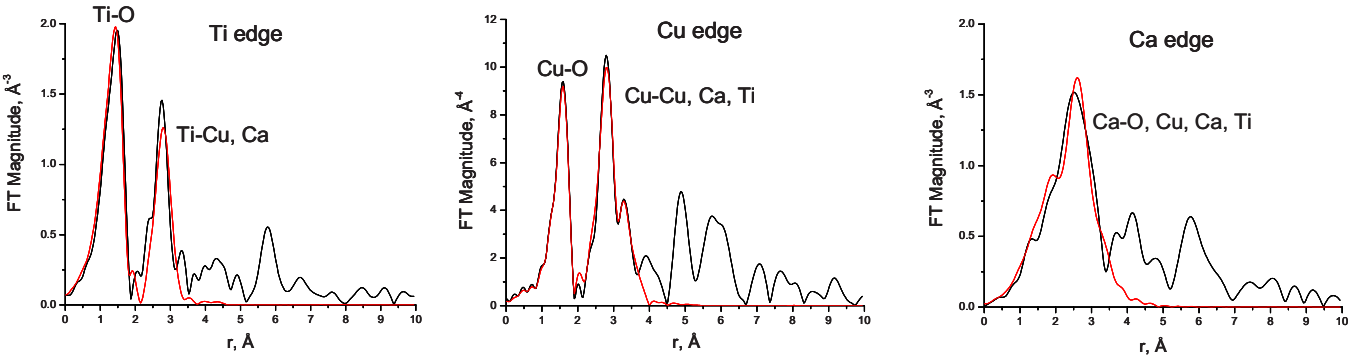

FIG. 8. (Color online) The Ti *K*, Cu *K*, and Ca *K* edges of the EXAFS data and their theoretical fits.

shows the EXAFS data of Ti, Cu, and Ca *K*-edge superimposed on their theoretical fits. As explained above, the best-fit values of $N_{\text{Cu-Ca}}$ and $N_{\text{Ca-Cu}}$ can either communicate partial order (when $1.5<N_{\text{Cu-Ca}}<2$ and $4.5<N_{\text{Ca-Cu}}<6$) coupled with the preservation of the long-range order or reveal macroscopic compositional fluctuations (when $N_{\text{Cu-Ca}}$ and $N_{\text{Ca-Cu}}$ are outside of the above ranges) without long-range order.[59] The coordination numbers, based on the best-fit results and obtained by concurrent EXAFS modeling of Ti, Ca, and Cu data, as well as the bond lengths are summarized in Table VI. We found that the Cu-Ca and Ca-Cu coordination numbers, $N_{\text{Cu-Ca}}=2.8\pm1.0$ and $N_{\text{Ca-Cu}}=2.4\pm1.6$, respectively, obtained by EXAFS significantly deviate from those (2.0 and 6.0, respectively) expected in the idealized, homogeneous CCTO with the *Im*3 structure. Such deviation cannot be explained by randomizing Cu and Ca at their sites within *the same* unit cell (in the random alloy $N_{\text{Ca-Ca}}=1.5$ and $N_{\text{Ca-Cu}}=4.5$). Thus, our conclusion from this observation is that the randomization occurred at the length scale of a few unit cells (some—Cu rich and some—Ca rich), rendering a possibility of forming nanoscale regions with antisite chemical disorder. We would like to emphasize that the signature of the nanoscale disorder is not the Cu-Ca and Ca-Cu coordination numbers alone but also the differences in the Ti-Cu and Ti-Ca distances, as well as the Cu-Cu, Cu-Ca, and Ca-Ca distances not observed by XRD measurements, which were obtained independently from the coordination numbers. Indeed, in a homogeneous alloy, the Cu-Ca and Ti-Ca distances should be longer than Cu-Cu and Ti-Cu, respectively, due to the larger size of Ca ion relative to Cu. In this system, we obtain the opposite effect (Table VI). All the information available from EXAFS, therefore, points to a structural disorder that is inconsistent with the ideal $Im\bar{3}$ structure. We found no evidence of enhanced (compared to thermal disorder) values of Cu-O, Ti-O, or Ca-O bond-length disorder, thus ruling out measurable oxygen-atom disorder and, in turn, its possible role in conductivity.

As a control, a model of stoichiometric CCTO without defects was also fit simultaneously to all of the available edge data. Although the reduced chi squared for the fit of this model to the multiple data sets was comparable with that for the previous model where antisite defects were allowed, the latter model resulted in a worse fit quality for Cu *K* edge, the one most sensitive to the Cu/Ca substitution. Indeed, the Ca *K*-edge data were the worst quality with the lowest k_{max} (and thus the worst spatial resolution of all the data), and the Ti *K*-edge data are not sensitive to Ca/Ca substitution since Ti is the common atom in this system.

Here we explore in greater detail the model that contains the Ca/Cu antisite defects. In this model, the deviations in

TABLE VI. Structural results obtained from multiple-edge EXAFS data analysis compared with DFT data (pseudopotential LSDA calculations).

Bond	N_{exp}	$N_{\text{th}}(x=0)$	$N_{\text{th}}(x=1)$	N_{DFT}	R_{DFT} (Å)	R_{EXAFS} (Å)	R_{XRD} (Å)	σ^2 (Å^2)
Ti-O	6	6	6	6	1.953	1.96(2)	1.964	0.0072(28)
Cu-O	4	4	4	4	1.968	1.971(4)	1.971	0.0041(3)
Cu-O	4	4	4	4	2.786	2.80(5)	2.789	0.015(10)
Cu-O	4	4	4	4		3.25(1)	3.269	0.013(30)
Ca-O	12	12	12	12	2.552	2.56(3)	2.606	0.024(6)
Ti-Cu	6	6	6	5	3.194	3.22(2)	3.206	0.0079(10)
Ti-Ca	2	2	2	3	3.205	3.17(4)	3.206	0.0043(35)
Cu-Cu	2.8(1)	4.5	4	4 or 2	3.704	3.77(2)	3.703	0.0040(20)
Cu-Ca	3.2(1)	1.5	2	4 or 6	3.679	3.70(2)	3.703	0.0038(29)
Ca-Cu	2.4(1.6)	4.5	6	4 or 6	3.679	3.70(2)	3.703	0.0038(29)
Ca-Ca		1.5	0	2	3.739			

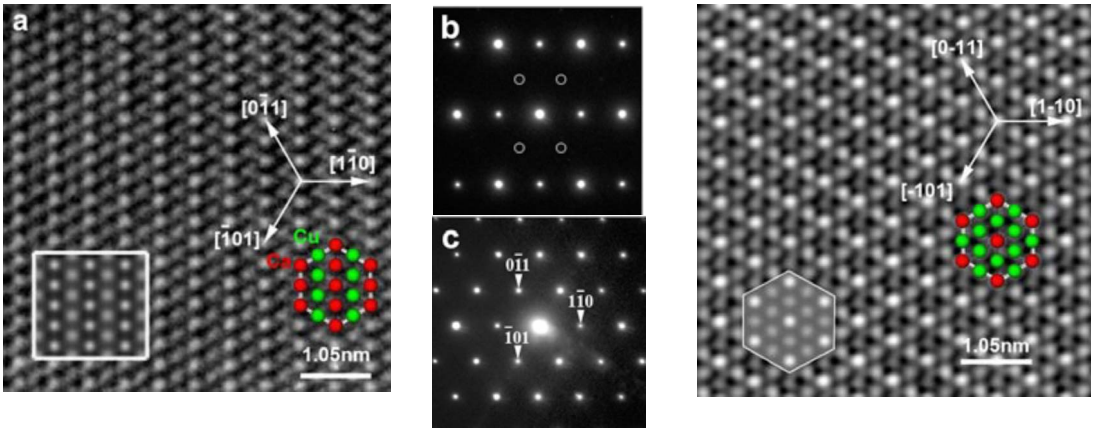

FIG. 9. (Color online) (a) High-resolution image of an unusually large Ca-rich region in CCTO taken along the [111] projection. The boxed area is the simulation using the model on the right. (b) Electron-diffraction pattern from the Ca-rich area showing broken a threefold symmetry. Open circles represent the missing 0–11 and −101 reflections. (c) Electron-diffraction pattern from a stoichiometric region of CCTO showing a threefold symmetry. (d) High-resolution image of perfect CCTO observed along the same orientation as (a) The boxed area is the simulation using the model on the right (for simplicity, only Ca and Cu are drawn).

coordination numbers from those expected in homogeneous CCTO indicate the presence of a Ca-rich phase $Ca_xCu_{1-x}TiO_3$, where $x>0.25$, as well as Cu-rich phase where $x<0.25$, suggesting the presence of local compositional and structural disorder with Ca on the Cu sites. Both types of phases must be present in the sample, along with the stoichiometric phase ($x=0.25$), since our measurements show that the overall sample composition is stoichiometric ($x=0.25$). Since both Cu and Ca edge analyses points to the presence of Ca-rich regions, we suggest that the Cu-rich regions are more disordered, or have reduced dimensionality, than the Ca-rich ones, which might reflect the smaller size of the Cu ion relative to Ca. This conclusion is consistent with our TEM observations. Figure 9(a) shows a high-resolution image from an unusually large Ca-rich region in the CCTO single crystal taken along the [111] projection. The boxed area is the simulation using the model on the right. A corresponding electron-diffraction pattern from the area is shown in Fig. 9(b), with a clear broken threefold symmetry, similar to the observations reported previously. The open circles represent the missing (0–11) and (−101) reflections, being consistent with the image. For comparison, in Fig. 9(c) we include the $(111)^*$ diffraction pattern from the stoichiometric ordered CCTO with threefold symmetry. The corresponding high-resolution image is shown in Fig. 9(d). The model and the simulation of the structure are also included.

Although we observed a Ca-rich region using electron diffraction and imaging, we have not convincingly detected the Cu-rich regions. There were two reasons: (1) as EXAFS suggested that the Cu-rich must be low dimensional, i.e., a small Cu-rich disordered region embedded in the ordered matrix is difficult to see in a projected image, especially considering the small difference in scattering amplitude between Ca and Cu; and (2) from a diffraction point of view, the substitution of Ca with Cu does not significantly alter the crystal symmetry and change the extinction of the reflections and is thus difficult to detect in diffraction. Our TEM spectroscopy measurements [energy dispersive x-ray (EDX) and electron-energy-loss spectroscopy (EELS)] of Cu-rich regions were inconclusive. This can be attributed to their low dimension, thus low-concentration difference from the matrix through the sample thickness.

TABLE VII. Summary of the PDF refinement results obtained by PDFGUI program for 300 K neutron data. Crystallographic $Im\bar{3}$ model refinement yields $a=7.4011(3)$ Å, $x(O)=0.3027(2)$, $y(O)=0.1789(2)$, $U_{ISO}(Ca)=0.0050(6)$ Å^2, $U_{ISO}(Cu)=0.0050(2)$ Å^2, $U_{ISO}(Ti)=0.0044(2)$ Å^2, and $U_{ISO}(O)=0.0047(1)$ Å^2. Three models including chemical disorder with respect to crystallographic stoichiometric model are compared. Refined parameters in these models are replacement (or off-stoichiometry) parameter, d, $U_{iso}(Ca)$, and $U_{iso}(Cu)$. Structural parameters are kept fixed to crystallographic values. Denotations are listed as follows: Crystallographic=crystallographic with nominal stoichiometry, Antisite=chemical disorder on Cu and Ca sites with nominal stoichiometry, E-Cu=excess Cu on Ca site (nonstoichiometric), E-Ca=excess Ca on Cu site (nonstoichiometric). See text for details.

Parameter\model	Crystallographic	Antisite	E-Cu	E-Ca
$U_{ISO}(Ca)$ (Å^2)	0.0050(6)	0.0056(7)	0.0044(7)	0.0053(6)
$U_{ISO}(Cu)$ (Å^2)	0.0050(2)	0.0048(2)	0.0050(3)	0.0048(2)
d		0.07(3)	−0.11(6)	0.09(3)
R_w	0.1351	0.1347	0.1348	0.1343

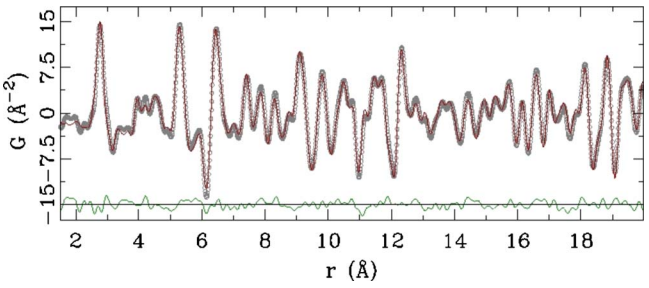

FIG. 10. (Color online) Typical CCTO PDF model fit: experimental PDF at 300 K (open circles), antisite model (solid line), and corresponding difference curve (offset for clarity).

In short, although we did not observe Ti-related disorder, we do find that a model with a disordered phase with Cu/Ca substitution, suggested by the TEM and electron-diffraction results, is consistent with the EXAFS data. Similar nanoscale phases were previously established with EXAFS in analogous systems.[29,60]

E. Analysis of neutron PDF data

The neutron powder-diffraction PDF results from the RT refinements based on the method we discussed in Sec. II D are tabulated in Table VII. To model the data we used the crystallographic ($Im\bar{3}$) model. This was refined to the PDF data to obtain structural parameters, in agreement with the previous study.[9] Then several models incorporating antisite disorder were attempted to allow the exchange of Ca and Cu ions. The antisite model preserved the nominal stoichiometry by only allowing switches of Cu and Ca ions. We also tried models where Cu was allowed to reside on Ca sites, Cu_{Ca}, and vice versa, without changing the composition of the unaffected site that results in a change in overall stoichiometry of the sample. In each case, a defect parameter, d, was defined. For the antisite model $d=O(Cu_{Ca})$, where $O(X_y)$ is the occupancy of X atoms on Y-atom sites, with the further constraints $O(Cu_{Cu})=1-d$, $O(Ca_{Cu})=0.33d$, and $O(Ca_{Ca})=1-0.33d$. This retains the overall stoichiometry because there are three copper sites for every Ca site. We also tried two models for uncompensated antisite defects. The E-Cu model has $d=O(Cu_{Ca})$ with the further constraint $O(Ca_{Ca})=1-d$ to ensure full occupancy of the Ca site by either Ca or Cu, and the occupancies of the copper sites set to 1. For completeness we also define an E-Ca model with $d=O(Ca_{Cu})$, $O(Ca_{Ca})=1-d$ and the Cu site fully occupied with copper. Refinements were first carried out with $d=0$, which is the ideal crystallographic model. This process reproduced the results presented in Ref. 9, with all refined parameters being within two standard deviations of the values reported in Ref. 9) as expected. The parameter d was then allowed to refine in addition to the free variables from the crystallographic models. Refinements were carried out over a range of r to 20 Å on data with the following temperatures: 50, 100, 150, and 200 K, and room temperature. For temperatures at 300 K and below, we expect negligible diffusion of cations and so the cation distribution in the samples must be the same at all temperatures. However, the complementary data sets provide independent measurements and should give consistent results for d.

TABLE VIII. Refined values of the defect parameter, d (see text for details) for the different models and different measurement temperatures refined.

T (K)	Antisite	E-Ca	E-Cu
300	0.07(3)	0.09(3)	−0.11(6)
200	0.01(3)	0.04(3)	−0.11(6)
150	−0.01(3)	0.02(3)	−0.10(6)
100	−0.01(3)	0.01(3)	−0.09(6)
50	−0.04(3)	−0.02(3)	−0.06(6)

A typical CCTO PDF model with antisite disorder fit with the experimental data at 300 K is shown in Fig. 10. The refined values of the defect parameter, d, for all temperatures and models are summarized in Table VIII. For the 300 K data, the agreement factors are slightly improved for all the antisite models with small positive disorder parameters, d, refined for the antisite and E-Ca models (Ca defects on Cu sites). However, the refinements to the lower-temperature data sets all converge to d values that are not significantly different from zero, suggesting that the neutron-diffraction data of the powder sample do not support the presence of significant antisite defects within the precision of the measurement. Based on the estimated errors in the refinement, the uncertainty on the refined d parameter is ~3%, which may be considered as a lower-bound because it does not take into account systematic errors and parameter correlations in the refinement which both contribute to the uncertainty. The neutron data therefore do not contradict the TEM and EXAFS observations but they do place an upper bound on the extent of the effect. It is difficult to put a precise numerical value on this bound but based on the estimated uncertainties on the data we suggest it is certainly less than 10% and probably about ~5%. We note that in the case of the antisite defects, the PDF d parameter and EXAFS x parameter are defined the same way. The PDF data are not good enough to differentiate between stoichiometric and nonstoichiometric models for the antisite disorder and for the same reason, no models with short-range ordering of the defects were tried.

F. Formation energy of nonstoichiometric phases

The antisite disorder of Ca and Cu in CCTO seems unfavorable from chemical intuition based on their ionic radii (i.e., 0.57 Å for a 4-coordinate Cu^{2+} vs 1.34 Å for a 12-coordinate Ca^{2+}) and bond length (1.967 Å for Cu-O bond length vs 2.602 Å for Ca-O). To understand the energetics of various phases in CCTO, we calculated the total energy of three different phases, stoichiometric, Ca-rich, and Cu-rich phases, and compared their formation energies to examine their stabilities using LDA-based pseudopotential calculations. The formation energy for different phases can be defined as

$$E_{\text{form}}(Ca_xCu_{8-x}Ti_8O_{24}) = E_{\text{tot}}(Ca_xCu_{8-x}Ti_8O_{24}) - xE_{\text{tot}}(CaO) - (8-x)E_{\text{tot}}(CuO) - 8E_{\text{tot}}(TiO_2).$$

Here, $Ca_xCu_{8-x}Ti_8O_{24}$ represents the general form of system

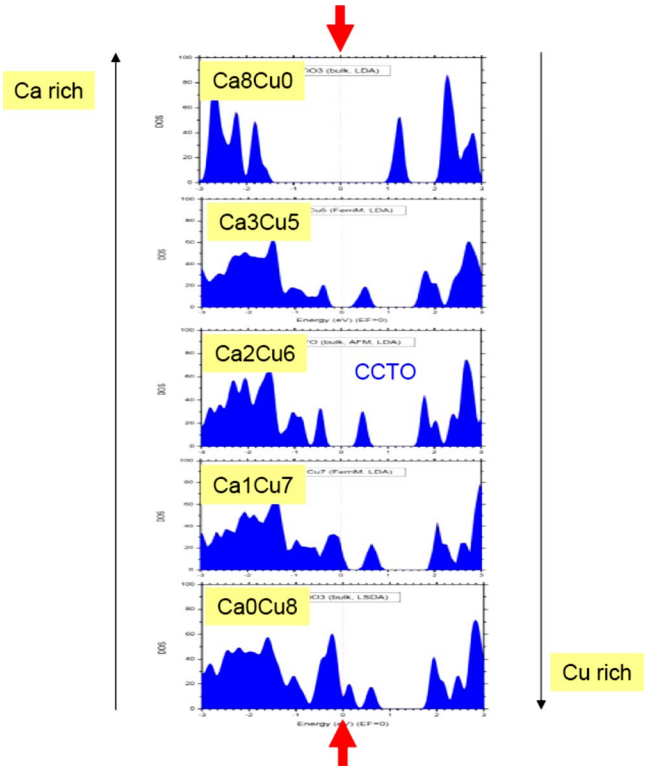

FIG. 11. (Color online) Density of states of $Ca_xCu_{8-x}Ti_8O_{24}$ as a function of composition calculated using pseudopotential localized spin-density approximation LSDA) with optimized geometry (top to bottom: $x=8$, 3, 2, 1, and 0). Stoichiometric $Ca_2Cu_6Ti_8O_{24}$ corresponds to $x=2$. Note, for $x \geq 2$ (top three phases), the system exhibits a insulating behavior with an energy gap near the Fermi level. For $x<2$, the system becomes metallic.

for various compositions ($x=1$, 2, and 3), E_{form} and E_{tot} is the formation energy and the total energy, respectively. We use CaO, CuO, and rutile TiO_2 as starting oxides that are commonly used in synthesis. We have

$$E_{form}(Ca_2Cu_6Ti_8O_{24}) = E_{tot}(Ca_2Cu_6Ti_8O_{24}) - 2E_{tot}(CaO) - 6E_{tot}(CuO) - 8E_{tot}(TiO_2) = -2.20 \text{ (eV/40 atom cell)},$$

$$E_{form}(Ca_3Cu_5Ti_8O_{24}) = E_{tot}(Ca_3Cu_5Ti_8O_{24}) - 3E_{tot}(CaO) - 5E_{tot}(CuO) - 8E_{tot}(TiO_2) = -2.39 \text{ (eV/40 atom cell)},$$

$$E_{form}(Ca_1Cu_7Ti_8O_{24}) = E_{tot}(Ca_1Cu_7Ti_8O_{24}) - E_{tot}(CaO) - 7E_{tot}(CuO) - 8E_{tot}(TiO_2) = +0.40 \text{ (eV/40 atom cell)}.$$

The results suggest that the formation of stoichiometric and Ca-rich CCTO are energetically favorable while that of the formation of Cu-rich CCTO is unfavorable. This means that the Ca-rich phase can grow bigger in size than the Cu-rich phase. In our calculations, the entire structure was relaxed without imposing any displacement constraints. The result is in full agreement with our EXAFS and TEM data that due to the small size of the Cu-rich phase we mainly observe only Ca-rich phase from the overall stoichiometric crystal (see Sec. III D 2).

G. Electronic properties of $Ca_xCu_{8-x}Ti_8O_{24}$ ($0 \leq x \leq 8$)

The total density of states of off-stoichiometric CCTO, i.e., $Ca_xCu_{8-x}Ti_8O_{24}$ ($0 \leq x \leq 8$), as a function of x were studied using pseudopotential LSDA (localized spin-density approximation) with optimized crystal geometry. The results are plotted in Fig. 11. (Note that the finite bandwidth of the Cu orbitals near the Fermi level results artificially from the periodicity of the disordered Cu in the calculation.) The AFM bulk stoichiometric $Ca_2Cu_6Ti_8O_{24}$ (i.e., $x=2$) phase clearly shows a ~0.5 eV band gap and is in good agreement with previous pseudopotential LSDA calculations.[6] From Ca-rich to Cu-rich phases, Fig. 11 clearly shows an increasing amount of Cu d orbitals residing near the Fermi level. For the Ca-rich phases (namely, with composition of $x>2$), there is an energy gap at the Fermi level and the gap remains till $x=2$, i.e., stoichiometric CCTO. On the other hand, as soon as Cu starts to occupy the Ca sites to form various Cu-rich phases (lower two panels), the associated d orbitals start to pile up at the Fermi level. The same trend is reproduced upon inclusion of a strong local interaction in Cu atoms via LSDA+U (Ref. 57) calculations within the full-potential linear APW methods.[54] In the LSDA+U calculations for stoichiometric antiferromagnetic CCTO, the Cu $3d$ states are more localized and the band gap is broadened to about 2 eV, which is in good agreement with experimental observations (>1.5 eV).[61] For the Cu-rich CCTO (e.g., for $x=1$, namely, $Ca_1Cu_7Ti_8O_{24}$), the LSDA+U calculations also show Cu states at the Fermi level from the Cu located in the Ca sites.

IV. DISCUSSION

A. Ca/Cu disorder

Our EXAFS and TEM results clearly suggest that there is a local Ca/Cu disorder in the CCTO single crystals that we studied. The obvious question we have was why neutron and x-ray diffraction experiments did not unambiguously identify but only give some evidence of such an antisite disorder.

In the $Im\bar{3}$ CCTO structure, the substitution of Cu at Ca sites and Ca at Cu sites result in changes only in the intensity of the *ooe* class of reflections (o and e refers to odd and even numbers, respectively) but does not result in any change to the *eee* reflections. Consequently, the normal least-squares refinement parameters for the entire data set are not very sensitive to the substitution when only limited numbers of reflections are collected. The change in agreement factors (goodness of fit) with and without 5% substitution is quite small. Even at 10% of substitution (20% of disordered regions), the agreement factor changes only from 1.32 to 2.24. To show the effects of the substitution on major reflections in the x-ray data, in Fig. 12 we plot calculated intensity vs 2θ scattering angles of powder diffraction for CCTO using MATERIALS STUDIO software with a wavelength $\lambda=0.154$ nm.

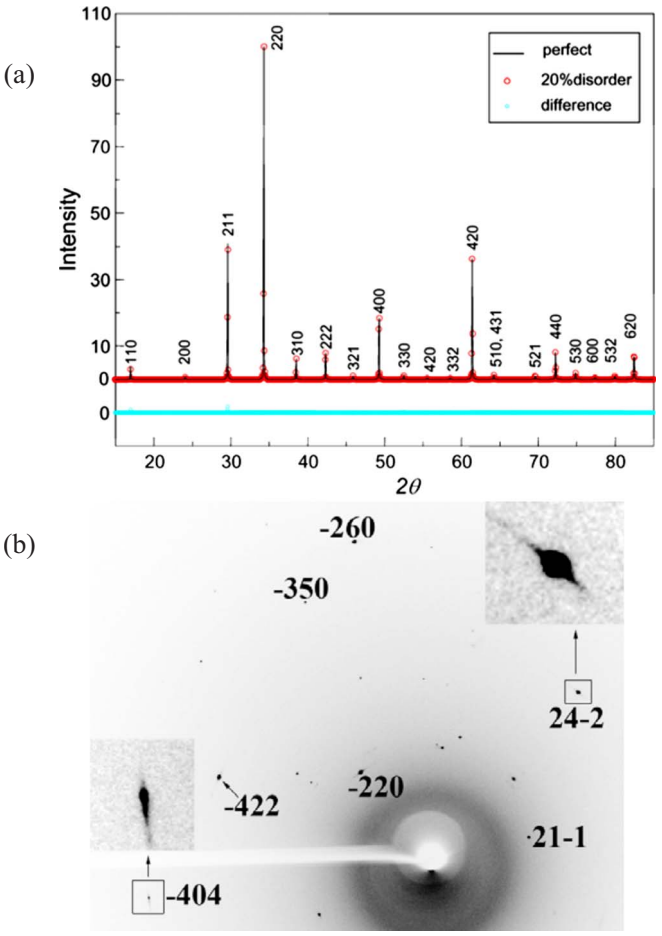

FIG. 12. (Color online) (a) Calculated intensity vs scattering angles of powder x-ray diffraction (XRD) pattern for CCTO using MATERIALS STUDIO software with wavelength l=0.154 nm. The solid lines are for perfect CCTO, the open circles are for CCTO with 10% swap of Ca with Cu, i.e., 20% of disordered regions. The difference, calculated by subtracting the intensity of disordered from that of perfect CCTO, is shown in blue. Note, visible difference only shown at the 110 and 211 reflections. Our accurate measurements of the structure factor of the two reflections suggest they deviate from the DFT calculation of the perfect CCTO. (b) X-ray diffraction pattern of CCTO single crystal recorded at room temperature, showing diffuse scattering surrounding some of the Bragg peaks.

The solid lines are for ideal stoichiometric CCTO, the crosses are for CCTO with a 10% swap of Ca with Cu, i.e., 20% of disordered regions. The difference, calculated by subtracting the intensity of the disordered from that of perfect CCTO, is shown in blue. The largest discrepancies are at the 110 and 211 reflections (our accurate measurements of the structure factor of the two reflections using PARODI also suggest they deviate from the DFT calculation of the perfect CCTO). It is evident that a small percentage of disorder in CCTO has a subtle change in the overall x-ray diffraction data. This is to be expected because of the small difference between Ca and Cu x-ray scattering factors.

In the refinement using perfect CCTO, the R1 and wR2 are 0.023 and 0.075, respectively. By simply introducing 5% exchange between Ca and Cu (corresponding to 10% disorder) without refinement the R1 increases to 0.028 while wR2 to 0.091. After further refinement, the R1 actually decreases to 0.018 while wR2 to 0.046. We note although the change in the R factors is not significant, it indeed indicates the possible existence of the disordered phase. We plan to perform an additional x-ray experiment with much high-order reflections [including diffuse scattering analysis, see Fig. 12(b)] to accurately determine the amount of the disordered phases.

It is interesting to note that at room temperature, our measurements using EXAFS, TEM, and PDF all point to the existence of small percent of Ca/Cu antisite disorder in CCTO, in particular, with detectable Ca-rich regions and undetectable Cu-rich regions. This is consistent with our DFT calculations based on the energy ground of the two phases. At lower temperatures, the Ca/Cu disorder seems much less measurable (90 K for TEM and 50–200 K for PDF measurements) and PDF analysis was inconclusive on the existence of the Ca/Cu disorder (see Sec. III E). The observed variation in Ca/Cu disorder at different temperatures may be an important factor that can be associated with low-temperature-dependent dielectric properties of CCTO, which shows a reduction in dielectric constant for certain frequencies at 100 K and below.

At current stage, it is not clear what the origin of the variation in Ca/Cu disorder at different temperatures is. Temperature-dependent EXAFS, QED, and high-resolution EELS measurements to explore temperature-dependent electronic structure and the dielectric function at much lower temperatures than 100 K as well as theoretical dynamical calculations such as molecular-dynamics simulations may help to address this question. Further studies can also include a joint EXAFS/PDF analysis on new data obtained from diffraction and spectroscopy measurements on identical samples, as suggested in Ref. 62. In the following, we discuss the possible mechanism of Ca/Cu disorder induced enhancement of dielectric response.

B. Temperature effects on ionicity and charge transfer

Structure factors measured by quantitative electron diffraction at different temperatures were used to understand the temperature effects in the CCTO. To cancel the Debye-Waller factor term, all the structure factors were converted to 0 K for comparison. We noticed that the structure factor of the (200) reflection increases ~2%, from 18.96 at RT to 19.38 at 90 K. By comparing the hypothetical pure ionic and neutral-atom (procrystal) models, our calculations show that among the six measurable low-order structure factors in CCTO, only the (200) reflection is very sensitive to temperature. The (200) reflection is a measure of the degree of octahedral tilting in the double perovskite structure. The strong T dependence of this peak indicates a destruction of the long-range order of the octahedral tilts, via thermal fluctuations, and thus the weakening of the associated orbital ordering among the t_{2g} electrons. Such an observation is also seen in the PDF analyses.[9] As discussed below in more detail, such disruption of orbital ordering recovers the near degeneracy of the Cu electrons (in this case moving the t_{2g} states close to

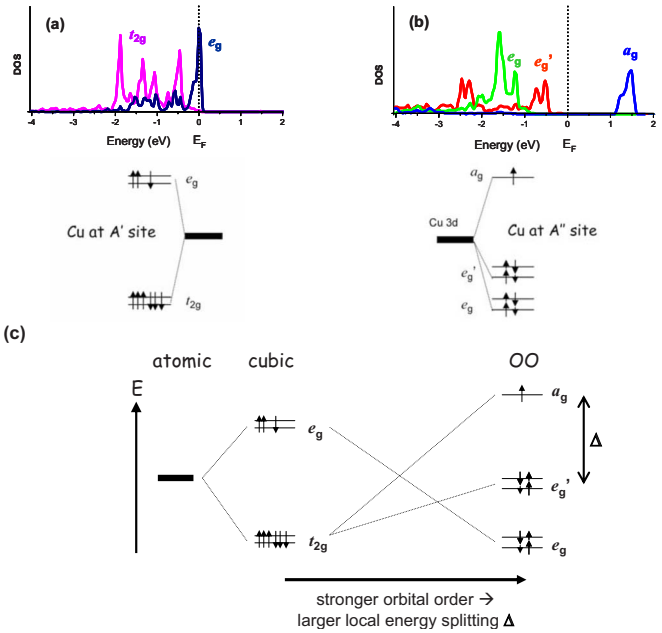

FIG. 13. (Color online) Local symmetry consideration of Cu orbitals showing the influence of antisite Ca/Cu order on the electronic structure in CCTO ($A'A''_3Ti_4O_{12}$). (a) Cubic symmetry (i.e., Cu at the A' site, or $Ca_3Cu_5Ti_8O_{24}$) and (b) lower symmetry (i.e., Cu at the A'' site as the ideal or ordered $CaCu_3Ti_4O_{12}$). The former hosts one hole in the triply degenerate t_{2g} complex and pins the chemical potential while the latter hosts one hole in the nondegenerate a_g orbital and allows the formation of a Mott insulator. The corresponding density of states obtained from DFT (LDA+U) calculations are also included, showing in perfect agreement with the local symmetry consideration [40-atom unit cell (space group $Pm\bar{3}$) in an AFM ground state for (b) and replacing Ca atom at the face center with Cu after relaxation for (a)]. (c) Evolution of local-orbital structure via lowering of the symmetry, from spherical (atomic) to cubic and to the orbital-ordered (OO) case. Clearly, the local energy splitting, Δ, of a_g and e'_g increases with strengthened orbital ordering.

the chemical potential from both above and below) which in turn would give a large electronic enhancement of the dielectric response and could provide a natural explanation of the experimentally observed increase in dielectric constant at higher temperature.

C. Electronic origin of giant dielectric response in CCTO

Our combined experimental and theoretical study leads to an interesting observation of large enhancement of dielectric response in CCTO via *electronic* contributions that are currently unnoticed in the literature. The above EXAFS and diffraction analyses provide strong evidence of nanoscale phase separations in CCTO with a mixture of stoichiometric (ordered) and nonstoichiometric (disordered) regions. The formation of these regions is further confirmed theoretically by their low formation energies obtained in our DFT calculations. In addition, the DFT results indicate a significant difference in the electronic structure in Cu-rich systems, favoring accumulation of Cu d states at the Fermi level (Fig. 11).

This interesting result of numerical calculations can be understood from the following robust local symmetry consideration. As illustrated in Fig. 13(a), under the local cubic point-group symmetry (as in the A' site), the five d orbitals of Cu splits into two sets, double-degenerate e_g and triple-degenerate t_{2g}. Therefore, the single hole in Cu^{2+} (d^9 configuration) resides in a complex of degenerate orbitals, pinning the chemical potential right in the middle of the degenerate orbitals, as shown in the local density of states of the A'-site Cu obtained in our DFT calculation. In contrast, the threefold degenerate t_{2g} orbitals further split into two distinct sets, a_g and e'_g for Cu located in the A'' sites, as shown in Fig. 13(b). This allows the system to lower its energy by having the hole in the highest nondegenerate a_g level, providing an opportunity for the formation of a Mott insulator based on our DFT calculation.

The apparent reason for the lower point-group symmetry of A'' site is the asymmetric positioning of the surrounding oxygen atoms associated with the TiO_6 octahedral tilting/distortion. However, recent first-principles theoretical studies of similar octahedral tilting/distortion in $LaMnO_3$,[63] Ca doped $LaMnO_3$,[64] and orbital ordering in Fe pnictides[65] revealed that even without the external lattice effects, the strong interactions among the $3d$ electrons make such a orbital degenerate system highly vulnerable against "orbital ordering," a spontaneous symmetry breaking with asymmetric orbital polarization and arrangement. Therefore, it is most likely that the octahedral tilting/distortion owes its microscopic origin, at least in part, to the underlying orbital ordering of the electrons.

The above robust symmetry consideration dictates that the A''-Cu should have partially filled degenerate orbital at the chemical potential if the symmetry were not broken by the orbital ordering (accompanied by the octahedral tilting/distortion). In that case, CCTO would have been a metal with divergent dielectric constant in the first place. It is precisely the splitting of the orbital degeneracy due to the orbital ordering that allows the insulating behavior of the system via the formation of a Mott insulator. Therefore, the electronic response of the system is expected to be unconventional and extreme caution must be exercised to avoid treating the system as a regular band insulator, such as the titanates, for example.

This microscopic insight suggests an interesting "extrinsic" feature that might explain the unusually large dielectric response. Since the insulating nature of the system is derived from the orbital ordering, any local disruption of the orbital ordering and the octahedral tilting/distortion, say via the introduction of A'-Cu or A''-Ca, would significantly reduce the local energy splitting, Δ, of the a_g and e'_g orbitals, as illustrated in Fig. 13(c). In addition, as discussed above, in the orbital-ordered structure, A' site has higher local point-group symmetry and can introduce degenerate orbitals right at the chemical potential ($\Delta \rightarrow 0$). Taking into account the first-moment sum rule, the dynamical spectral weight of the interorbital excitations across the gap is proportional to $1/\Delta$ while the Kramers-Kronig transform dictates the low-frequency dielectric function to be proportional to the dy-

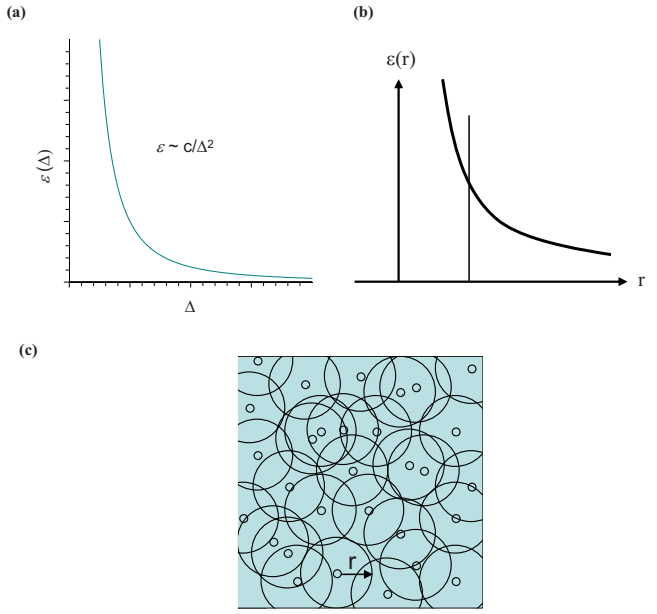

FIG. 14. (Color online) Illustration of enhancement of electronic dielectric response via proximity effects around A'-Cu. (a) $1/\Delta^2$ enhancement of the local dielectric constant for Cu atoms with disrupted orbital ordering. (b) The proximity effects of the dielectric constant around A'-Cu. At short distance ($r \to 0$) from the A'-Cu sites, the dielectric constant diverges quickly as the gap shrinks. (c) The proximity effects in a system with randomly distributed chemical disorder (disordered bubbles). If the occurrence of A'-Cu spreads throughout the sample without much clustering, as suggested by our EXAFS analysis, there can be very little region left unaffected by the proximity effects, giving rise to a significant enhancement of the total dielectric constant.

namical spectral weight multiplied by inverse of the excitation frequency. Together, one expects qualitatively a significant enhancement of the dielectric constant proportional to $1/\Delta^2$, as shown in Fig. 14(a).

Following the above rigorous analysis, we suggest the following inhomogeneous picture of enhanced *electronic* dielectric response. Near A'-Cu, the local dielectric response should be greatly enhanced from coupling to the degenerate orbitals of A'-Cu ($\Delta \to 0$) and the variation in significantly reduced Δ resulting from disruption of orbital ordering of the surrounding A''-Cu. The local dielectric response consists of a profile of singularly large value centered at each A'-Cu, with a smooth decay at larger distance [Fig. 14(b)]. Formulated in a continuous model, it is apparent the bulk dielectric function $\varepsilon_{\text{tot}}^{-1} = \frac{1}{V}\int \varepsilon^{-1}(x) d^3x$ is ultimately controlled by the regions with small local response. As illustrated in Fig. 14(c), given a random distribution of A'-Cu and A''-Ca and a large enough radius of the enhancement, the bulk dielectric response can be boosted easily by several order of magnitudes. That is, the above proximity effect can lead to a large dielectric response, given only a very small portions of the bulk that are far from all the A'-Cu sites, as indicated by our EXAFS data, to possess small enough local dielectric response that contribute to the integral.

This picture also naturally resolves a puzzling dilemma existing in some of the conventional extrinsic pictures[7] involving metallic domains with insulating boundaries in which a very small volume fraction ($\sim 10^{-3}$) of insulator is needed while the insulating boundaries have to fully cover the metallic domains in order to keep the system insulating. If such picture were to be realized, an insulating "blocking layer" to make the sample insulating would be unavoidable, which however was not observed in any of our measurements. This difficulty does not enter in our picture since the region near A'-Cu are still well insulating ($\Delta > 0$) in terms of transport (determined by states at the chemical potential) but with large dielectric response (controlled by all low-energy states with $\Delta \ll 1$.)

Our interpretation also provides a natural scenario for the well-known puzzle why the dielectric response of $CdCa_3Ti_4O_{12}$ is found two orders of magnitude lower than CCTO.[61] Cd and Ca are isoelectronic in these systems, with a very similar chemical size, and thus pure-phase Cd-CTO and CCTO have almost identical electronic structure, as confirmed by a previous theoretical study.[41] It is thus a great surprise that their dielectric response is so different. Now, since disorder in materials is controlled by complicated nonequilibrium process of crystal growth, the disorder in these two similar materials can be very different. Our picture suggests that either the degree of disordered A'-Cu is less in CdCTO or the disordered A'-Cu atoms form larger cluster (thus leaving larger volume fraction with small dielectric response). Future experimental verification of this issue will provide an unambiguous confirmation of our picture.

We note that the above novel picture of extrinsic effect is based on the proximity effect of metallic behavior in terms of dielectric response, not transport, of a disordered orbital-ordered Mott insulator, and is substantially different from the physics in a conventional band insulator such as conventional ferroelectric compounds. The validity of this strongly correlated picture can be experimentally verified by, for example, direct observation of these low-energy excitations via large-q inelastic x-ray scattering, which is capable of probing transition in atomic length scale or local dielectric profile with high-resolution low-energy electron-energy-loss spectroscopy measurement. Similar idea can be applied to the search for high dielectric materials by introducing disorders in other families of strongly correlated degenerate Mott insulators, such as the manganites or the vanadium oxides.

V. CONCLUSIONS

In summary, using experimental techniques that are sensitive to local disorder, we found that there exist small amount of off-stoichiometric nanoscale regions in CCTO single crystals. The measurement and detection are not trivial largely due to the low concentration and small size of the defect regions. Nonetheless, theoretical calculations based on density-functional theory suggest a large metal-like local *electronic* dielectric response near the disordered Cu atoms, as a consequence of the recovery of degeneracy of the open t_{2g} shell and the disruption of the long-range orbital order. Bulk measurements of local structure indicate that the defective regions constitute $<10\%$ of the sample. Because of the

difficulty of quantifying nanoscale defects at such low levels, further work will be required to establish that this mechanism is operative in $CaCu_3Ti_4O_{12}$. However, our results demonstrate that local atomic substitution or disorder can induce a dramatic change in the local dielectric behavior in strongly correlated systems with orbital freedom, and point to an innovative way in searching for fascinating properties in correlated materials, including perovskite transition-metal oxides.

ACKNOWLEDGMENTS

We thank Morrel H. Cohen, David Vanderbilt, Weiguo Yin, and Peter Stephens for stimulating discussions. A.I.F. acknowledges support by the U.S. Department of Energy, Office of Basic Energy Science, Grant No. DE-FG02-03ER15476. Work at Brookhaven was supported by the U.S. Department of Energy, Office of Basic Energy Science, under Contract No. DE-AC02-98CH10886 and DOE-CMSN.

*Corresponding author. zhu@bnl.gov

[1] M. A. Subramanian, D. Li, N. Duan, B. Reisner, and A. W. Sleight, J. Solid State Chem. **151**, 323 (2000).
[2] A. P. Ramirez, M. A. Subrmananian, M. Gardel, G. Blumberg, D. Li, T. Vogt, and S. M. Shapiro, Solid State Commun. **115**, 217 (2000).
[3] C. C. Homes, T. Vogt, S. M. Shapiro, S. Wakimoto, and A. P. Ramirez, Science **293**, 673 (2001).
[4] H. C. Li, W. Si, A. D. West, and X. X. Xi, Appl. Phys. Lett. **73**, 464 (1998).
[5] G. A. Samara and L. A. Boatner, Phys. Rev. B **61**, 3889 (2000).
[6] L. He, J. B. Neaton, M. H. Cohen, D. Vanderbilt, and C. C. Homes, Phys. Rev. B **65**, 214112 (2002).
[7] M. H. Cohen, J. B. Neaton, L. He, and D. Vanderbilt, J. Appl. Phys. **94**, 3299 (2003).
[8] L. Wu, Y. Zhu, S. Park, S. Shapiro, G. Shirane, and J. Tafto, Phys. Rev. B **71**, 014118 (2005).
[9] E. S. Božin, V. Petkov, P. W. Barnes, P. M. Woodward, T. Vogt, S. D. Mahanti, and S. J. L. Billinge, J. Phys.: Condens. Matter **16**, S5091 (2004).
[10] Y. Zhu and J. Tafto, Philos. Mag. B **75**, 785 (1997).
[11] J. Taftø, Y. Zhu, and L. Wu, Acta Crystallogr., Sect. A: Found. Crystallogr. **54**, 532 (1998).
[12] L. Wu, Y. Zhu, and J. Tafto, Micron **30**, 357 (1999).
[13] Y. Zhu, L. Wu, and J. Tafto, Microsc. Microanal. **9**, 442 (2003).
[14] L. Wu, Y. Zhu, T. Vogt, H. Su, and J. W. Davenport, Phys. Rev. B **69**, 064501 (2004).
[15] J. M. Zuo, M. O'Keeffe, P. Rez, and J. C. H. Spence, Phys. Rev. Lett. **78**, 4777 (1997).
[16] J. M. Zuo, M. Kim, M. O'Keeffe, and J. C. H. Spence, Nature (London) **401**, 49 (1999).
[17] A. P. Hamersley (1994) FIT2D program; A. P. Hammersley, ESRF Internal Report No. EXP/AH/95-01, 1995 (unpublished).
[18] Z. Otwinowski and W. Minor, *Methods in Enzymology*, Macromolecular Crystallography Part A Vol. 276, edited by C. W. Carter, Jr. and R. M. Sweet (Academic Press, New York, 1997), pp. 307–326; J. Zaleski, G. Wu, and P. Coppens, J. Appl. Crystallogr. **31**, 302 (1998).
[19] G. M. Sheldrick, *SHELXTL Reference Manual* (Bruker AXS, Madison, Wisconsin, 1993).
[20] E. D. Stevens and P. Coppens, Acta Crystallogr., Sect. A: Cryst. Phys., Diffr., Theor. Gen. Crystallogr. **32**, 915 (1976).
[21] J.-C. Zheng, L. Wu, Y. Zhu, and J. W. Davenport, J. Appl. Crystallogr. **38**, 648 (2005).
[22] H. K. Hansen and P. Coppens, Acta Crystallogr., Sect. A: Cryst. Phys., Diffr., Theor. Gen. Crystallogr. **34**, 909 (1978).
[23] R. F. Stewart, M. A. Spaceman, and C. Flensburg, *VALRAY User's Manual* (Carnegie Mellon University and University of Copenhagen, Pittsburgh, PA, 2000).
[24] E. Clementi and C. Roetti, in *Atomic Data and Nuclear Data Tables*, edited by K. Way (Academic Press, New York, 1974), Vol. 14, pp. 177–478.
[25] A. Frenkel, E. A. Stern, A. Voronel, M. Qian, and M. Newville, Phys. Rev. Lett. **71**, 3485 (1993).
[26] A. I. Frenkel, M. H. Frey, and D. A. Payne, J. Synchrotron Radiat. **6**, 515 (1999).
[27] A. I. Frenkel, V. Sh. Machavariani, A. Rubshtein, Yu. Rosenberg, A. Voronel, and E. A. Stern, Phys. Rev. B **62**, 9364 (2000).
[28] P. Pfalzer, J. Will, A. Naterprov, M. Klemm, S. Horn, A. I. Frenkel, S. Calvin, and M. L. denBoer, Phys. Rev. B **66**, 085119 (2002).
[29] A. I. Frenkel, D. M. Fanning, D. L. Adler, I. K. Robinson, and J. O. Cross, *The 5th Williamsburg Workshop on First-Principles Calculations for Ferroelectrics*, Williamsburg, Virginia, 1-4 February 1998, AIP Conf. Proc. No. 436 (AIP, New York, 1998), p. 96.
[30] A. I. Frenkel, D. M. Pease, G. Giniewicz, E. A. Stern, D. L. Brewe, M. Daniel, and J. Budnick, Phys. Rev. B **70**, 014106 (2004).
[31] A. I. Frenkel, Y. Feldman, V. Lyahovitskaya, E. Wachtel, and I. Lubomirsky, Phys. Rev. B **71**, 024116 (2005).
[32] A. I. Frenkel, D. M. Pease, J. Budnick, P. Metcalf, E. A. Stern, P. Shanthakumar, and T. Huang, Phys. Rev. Lett. **97**, 195502 (2006).
[33] E. A. Stern, M. Newville, B. Ravel, Y. Yacoby, and D. Haskel, Physica B **208-209**, 117 (1995).
[34] S. I. Zabinsky, J. J. Rehr, A. Ankudinov, R. C. Albers, and M. J. Eller, Phys. Rev. B **52**, 2995 (1995).
[35] A. V. Kolobov, P. Fons, A. I. Frenkel, A. L. Ankudinov, J. Tominaga, and T. Uruga, Nature Mater. **3**, 703 (2004).
[36] P. Shanthakumar, M. Balasubramanian, D. Pease, A. I. Frenkel, D. Potrepka, J. Budnick, W. A. Hines, and V. Kraizman, Phys. Rev. B **74**, 174103 (2006).
[37] M. S. Nashner, A. I. Frenkel, D. L. Adler, J. R. Shapley, and R. G. Nuzzo, J. Am. Chem. Soc. **119**, 7760 (1997).
[38] B. Bochu, M. N. Deschizeaux, J. C. Joubert, A. Collomb, J. Chenavas, and M. Marezio, J. Solid State Chem. **29**, 291 (1979).
[39] Y. J. Kim, S. Wakimoto, S. M. Shapiro, P. M. Gehring, and A. P. Ramirez, Solid State Commun. **121**, 625 (2002).
[40] S. G. Ebbinghaus, A. Weidenkaff, and R. J. Cava, J. Solid State Chem. **167**, 126 (2002).

[41] L. X. He, J. B. Neaton, D. Vanderbilt, and M. H. Cohen, Phys. Rev. B **67**, 012103 (2003).
[42] S. H. Byeon, M. W. Lufaso, J. B. Parise, P. M. Woodward, and T. Hansen, Chem. Mater. **15**, 3798 (2003).
[43] D. Capsoni, M. Bini, V. Massarotti, G. Chiodelli, M. C. Mozzatic, and C. B. Azzoni, J. Solid State Chem. **177**, 4494 (2004).
[44] S. Y. Chung, Appl. Phys. Lett. **87**, 052901 (2005).
[45] W. Wong-Ng, J. Suh, and J. A. Kaduk, Powder Diffr. **20**, 193 (2005).
[46] Y. Zhu, J. C. Zheng, L. Wu, A. I. Frenkel, J. Hanson, P. Northrup, and W. Ku, Phys. Rev. Lett. **99**, 037602 (2007).
[47] T. Egami and S. J. L. Billinge, *Underneath the Bragg Peaks: Structural Analysis of Complex Materials* (Pergamon, NewYork/Elsevier, Oxford, 2003).
[48] R. A. Young, *The Rietveld Method, International Union of Crystallography Monographs on Crystallography* (Oxford University Press, Oxford, 1993), Vol. 5.
[49] C. L. Farrow, P. Juhas, J. W. Liu, D. Bryndin, E. S. Božin, J. Bloch, Th. Proffen, and S. J. L. Billinge, J. Phys.: Condens. Matter **19**, 335219 (2007).
[50] Th. Proffen, R. G. DiFrancesco, S. J. L. Billinge E. L. Brosha, and G. H. Kwei, Phys. Rev. B **60**, 9973 (1999).
[51] T. Proffen, V. Petkov, S. J. L. Billinge, and T. Vogt, Z. Kristallogr. **217**, 47 (2002).
[52] P. Hohenberg and W. Kohn, Phys. Rev. **136**, B864 (1964); W. Kohn and L. J. Sham, *ibid.* **140**, A1133 (1965).
[53] J. M. Soler, E. Artacho, J. D. Gale, A. García, J. Junquera, P. Ordejón, and D. Sánchez-Portal, J. Phys.: Condens. Matter **14**, 2745 (2002).
[54] P. Blaha, K. Schwarz, G. K. H. Madsen, D. Kvasnicka, and J. Luitz, *WIEN2K, An Augmented Plane Wave PlusLocal Orbitals Program for Calculating Crystal Properties* (Vienna University of Technology, Vienna, Austria, 2001).
[55] J. P. Perdew and Y. Wang, Phys. Rev. B **45**, 13244 (1992).
[56] J. P. Perdew, K. Burke, and M. Ernzerhof, Phys. Rev. Lett. **77**, 3865 (1996).
[57] V. I. Anisimov, I. V. Solovyev, M. A. Korotin, M. T. Czyżyk, and G. A. Sawatzky, Phys. Rev. B **48**, 16929 (1993).
[58] J. M. Zuo, Rep. Prog. Phys. **67**, 2053 (2004).
[59] J. M. Cowley, Phys. Rev. **138**, A1384 (1965).
[60] E. Prouzet, E. Husson, N. DeMathan, and A. Morell, J. Phys.: Condens. Matter **5**, 4889 (1993).
[61] C. C. Homes, T. Vogt, S. M. Shapiro, S. Wakimoto, M. A. Subramanian, and A. P. Ramirez, Phys. Rev. B **67**, 092106 (2003).
[62] S. J. L. Billinge and I. Levin, Science **316**, 561 (2007).
[63] W.-G. Yin and W. Ku, Phys. Rev. Lett. **96**, 116405 (2006).
[64] D. Volja, W.-G. Yin, and W. Ku, EPL **89**, 27008 (2010).
[65] C.-C. Lee, W.-G. Yin, and W. Ku, Phys. Rev. Lett. **103**, 267001 (2009).